Spectroscopic Measurements of Methane Solid−Gas Equilibrium Clapeyron Curve between 40 and 77 K

Patrice Cacciani,[†] Peter Čermák,[*,†] Cédric Pardanaud,[§] Gabriela Valentová,[‡] Jean Cosléou,[†] Céline Martin,[§] Stéphane Coussan,[§] Jennifer A. Noble,[†,§] Younes Addab,[§] Corinne Boursier,[∥] Pascal Jeseck,[∥] Mathieu Bertin,[∥] Jean-Hugues Fillion,[∥] and Xavier Michaut[∥]

[†]Laboratoire de Physique des Lasers, Atomes et Molécules, Université de Lille, CNRS, UMR 8523, 59655 Villeneuve d'Ascq, France

[‡]Department of Experimental Physics, Faculty of Mathematics, Physics and Informatics, Comenius University, 84248 Bratislava, Slovakia

[§]Aix Marseille Université, CNRS, PIIM, Marseille, France

[∥]Sorbonne Université, Observatoire de Paris, Université PSL, CNRS, LERMA, F-75005 Paris, France

ABSTRACT: The infrared gas-phase absorption spectrum of methane was used to determine its Clapeyron solid−gas equilibrium curve in the 40−77 K temperature range. For comparative purposes and to obtain more reliable results, two different optical experimental setups were used. At higher temperatures (53−77 K), a single pass cryogenically cooled cell was coupled to a standard low-resolution Fourier transform infrared spectrometer. The second system was a state-of-the-art vertical-external-cavity surface-emitting laser tunable source operating at around 2.3 μm, combined with a 7 m path Herriott cell, to record methane absorption features down to 40 K. From the measurements, the vapor pressure curve $\ln(p/\text{Pa}) = -(1191.92 \pm 8.92)/(T/\text{K}) + (22.49 \pm 0.16)$ was derived in the range 40−77 K. This corresponds to a value of 9910 $\pm$ 75 J mol^{-1} for the sublimation enthalpy. The relation was validated down to 40 K, increasing our knowledge of the saturation pressure by 2 orders of magnitude. Data were compared with available pressure measurements from the literature, obtained by manometric or mass spectrometry techniques, and the sublimation enthalpy was compared with a thermodynamic approach based on heat capacity measurements in the solid and gas phases.
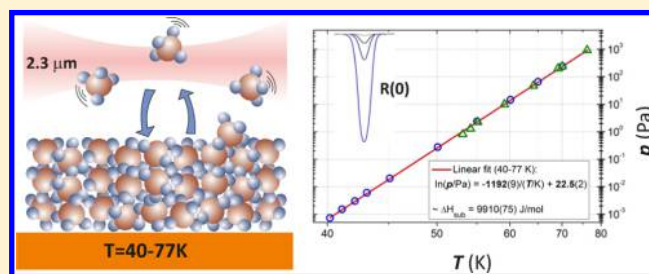
INTRODUCTION

Methane (CH$_4$) is a particularly interesting molecule of significant influence in many scientific fields, including atmospheric sciences, astrophysics, geoscience, combustion science, the chemical technology of hydrogen generation, and biotechnology. It is the main constituent of natural gas that power stations and industrial and residential users consume.[1] Additionally, there is a trend toward the increased use of methane as a fuel for appliances, vehicles, industrial applications, and power generation.[2] CH$_4$ plays an important role in the chemistry of the upper atmosphere, as it is the third most abundant greenhouse gas (after water and carbon dioxide) and thus responsible for significant global warming.[3] Methane is also present in the atmospheres of giant planets like Jupiter, Saturn, Uranus, and Neptune,[4] as well as their satellites, such as Titan.[5] More recently, its presence in small but significant quantities has been reported in the Martian atmosphere.[6] In all of these cases, the basic thermodynamic properties of methane are of crucial importance.

In this study, we present a determination of the Clapeyron solid−gas equilibrium curve for methane in the 40−77 K range. Commonly, the vapor pressure is measured using contact pressure probes. However, at low temperatures, where

the density of molecules in the gas phase is so low that the collisions with the walls become non-negligible in comparison with the intersample collisions, the so-called "thermal transpiration effect" prohibits manometric measurements.[7] The motivation for this work was to investigate the performance of optical measurements compared with these "conventional" contact methods, as applied to the case of methane. The main advantage is that the use of light as a probe allows for vacuum isolation of the studied sample in thermal and phase equilibrium at a given temperature. Second, both temperature and pressure of the sample can be retrieved from a single optical spectrum, significantly simplifying the experimental scheme. A similar approach has previously been applied to water, where the saturation pressure was measured below its triple point using highly accurate measurements from cavity ring down spectroscopy (CRDS).[8] Although in the CRDS experiment the low pressure sample was not measured at low temperature but rather flushed by nitrogen from a humidity generation system at room temperature, the

commonality with our setup is the measurement of a low molecular density with an appropriate spectroscopic method.

Despite the interest in methane in terms of its nuclear spin (NS) dynamics (e.g., ref 9) and the fact that several extensive reviews on methane vapor pressure have been published, few experimental vapor pressure measurements have been made below its triple point, $T_{TP} = 90.6941 \pm 0.0025$ K and $p_{TP} = (116.96 \pm 0.02) \times 10^{-2}$ Pa.[10] In these studies, pressure was determined using manometers in the case of Eucken et al.[11] and Armstrong et al.,[12] or using mass spectrometers by Tickner et al.[13] The temperature range of the sublimation was limited to 76.89−90.6, 53−90.6, and 47.5−90.6 K, respectively. These references can be found in the database of the National Institute of Standards and Technology Chemistry WebBook,[14] which provides the methane vapor pressure temperature curves for sublimation down to 50 K and for vaporization up to the critical point, $T_{CP} = 190.564 \pm 0.012$ K and $p_{CP} = 4.5922 \pm 0.002$ MPa.[10] Indirectly, the sublimation vapor pressure can also be retrieved from the calorimetric capacities, which can be measured with good precision and accuracy even at very low temperatures. This was done by Colwell et al.[15] for methane and its deuterated isotopologue CD_4 in the 4−90 K range. Comparison of pressure and sublimation enthalpy with our data will be discussed.

Our experimental work was aimed at establishing reliable vapor pressure data for methane below 77 K and extending the lower temperature boundary to 40 K (from the previous 47.5 K obtained by Tickner et al.[13]). To perform this task, we have combined data from two separate experiments. The "high-resolution setup" (HRS) laser source was a prototype frequency tunable vertical-external-cavity surface-emitting laser (VECSEL) operating in the 2.3 μm region coupled to a 7 m path length cryogenically cooled Herriott cell (HC)[16,17] and probed the lowest rotational levels of the $\nu_1 + \nu_2$, $\nu_1 + \nu_4$, $\nu_3 + \nu_4$, and $2\nu_2 + \nu_4$ combination bands of the $\nu_1(A)$, $\nu_2(E)$, $\nu_3(F)$, and $\nu_4(F)$ vibrational bands.[18] The second experiment, referred to hereafter as the "low-resolution setup" (LRS) was based upon a standard "low resolution" Bruker IFS66 Fourier transform infrared (FTIR) spectrometer with a simple path cell approximately 2 cm in length to cover the CH_4 absorption from the strongest ν_3 band, around 3 μm, to the components of the $\nu_1 + \nu_4$ and $\nu_2 + \nu_3$ combination bands, around 2.3 and 2.2 μm, respectively.[18] There were a number of reasons to combine these two experiments. In terms of sensitivity, due to the longer path length, the HRS offered a better signal-to-noise ratio down to low temperature but the accuracy was limited by the interferences in the signal, characteristic of Herriott cells.[17] On the other hand, although the LRS allowed the registration of the absorption signal only down to 55 K, its readings in the 60−77 K range were more accurate and served as absolute calibration for the HRS data. Second, as the low-resolution FTIR spectrometer ($\sim$0.1−10 cm^{-1}) is a common tool found in many research laboratories studying molecules in the solid or liquid phases, its ability to measure gas pressure (limits and error sources) could be considered as an interesting alternative to manometric measurements.

This paper is organized as follows: the first part is an overview of the methodology used to determine pressure and temperature from the optical absorption measurements. Part two details the two cryogenic experimental setups used to record the methane infrared absorption spectra. Part three gives the experimental results and their analysis in terms of pressure and sublimation enthalpy. This latter value is then compared to sublimation enthalpy derived from a thermodynamic approach using heat capacity measurements of the solid and gas phases, and finally, the vapor pressure curve including previous refs 11−13 is addressed. Some technical details regarding the LRS experiment are presented in the Appendix (i.e., the treatment of the interferogram and the determination of optical path length).

■ METHODOLOGY

The principle of the experiment is to retrieve both the pressure p and the temperature T from the absorption pattern imprinted onto the light beam passing through a gas sample at thermal and phase equilibrium. Therefore, by definition, the pressure retrieved is equal to the sample vapor pressure at the corresponding temperature. The following text briefly reviews the process of the extraction of p and T from the absorption spectra following the methodology used by the high-resolution transmission molecular absorption database (HITRAN).[18]

To quantitatively characterize the absorption of a given substance, we can use the dimensionless Napierian absorbance $A_{\eta\eta'}(\tilde{\nu})$. It describes the rate of light attenuation on the interaction path of length L at a given wavenumber $\tilde{\nu}$ due to the absorption by the transition between the lower state η and upper state η', separated by the energy difference $\tilde{\nu}_{\eta\eta'}$. The total absorbance for a substance of concentration n is then a composition of contributions $A_{\eta\eta'}$, active in the targeted spectral range

$$A(\tilde{\nu}) = \sum_{\forall(\eta' \leftarrow \eta)} A_{\eta\eta'}(\tilde{\nu}) = \sum_{\forall(\eta' \leftarrow \eta)} n \cdot L \cdot S_{\eta\eta'} \cdot \phi_{\eta\eta'}(\tilde{\nu} - \tilde{\nu}_{\eta\eta'}) \quad (1)$$

where the product $S_{\eta\eta'} \cdot \phi(\tilde{\nu} - \tilde{\nu}_{\eta\eta'})$ represents the rate of absorption by the molecule, with $S_{\eta\eta'}$ the strength of the transition and $\phi(\tilde{\nu} - \tilde{\nu}_{\eta\eta'})$ its normalized line shape.

In eq 1, the simplest variable to calculate is the concentration, from which the pressure dependence is obtained from the ideal gas law: $n = p/k_B T$, with k_B the Boltzmann constant. The line shape $\phi_{\eta\eta'}(\tilde{\nu} - \tilde{\nu}_{\eta\eta'})$ is, to a first order approximation, described by a Voigt function, in which the Lorentz component represents the pressure broadening and the Gauss component accounts for the Doppler broadening of the transition. For a sample composed of a single substance of molar mass M, the HITRAN database uses the following formulae to calculate the corresponding half widths at half-maximum (given in cm^{-1})

$$w_{Lor} = \left(\frac{T_{ref}}{T}\right)^{n_T} \cdot p \cdot \gamma_{self}(T_{ref}, p_{ref}) \quad (2)$$

$$w_{Gauss} = \frac{\tilde{\nu}_0}{c} \sqrt{2 \ln 2 \frac{RT}{M}} \quad (3)$$

where γ_{self} is the self-broadening coefficient for reference values of $T_{ref} = 296$ K and $p_{ref} = 1$ atm (as defined by the HITRAN database); n_T, the coefficient of temperature dependence; $\tilde{\nu}_0$, the transition wavenumber; c, the speed of light; and R, the molar gas constant. Finally, for a given molecule and transition, $S_{\eta\eta'}$ depends only on the temperature, as

Table 1. Selection of the Targeted CH_4 Lines with Their Parameters according to the HITRAN2016 Database[18]

transition							
band	br.(J,sym.)^a	$\tilde{\nu}_0{}^b$ (cm^{-1})	$S_{\eta\eta'}{}^c$ (cm mol^{-1})	$S_{err}{}^d$	$E_i{}^e$ (cm^{-1})	$\gamma_{self}{}^f$ (cm^{-1}/atm)	$\gamma_{err}{}^d$
ν_3	R(0,A$_1$)	3028.7523	9.210×10^{-20}	6	0	0.081	3
	R(1,F$_1$)	3038.4985	8.853×10^{-20}	6	10.4816	0.081	3
	R(2,F$_2$)	3048.1533	1.132×10^{-19}	6	31.4424	0.083	3
	R(2,E)	3048.1691	7.543×10^{-20}	6	31.4421	0.083	3
	R(3,A$_2$)	3057.6874	2.106×10^{-19}	6	62.8781	0.079	3
	R(3,F$_2$)	3057.7265	1.260×10^{-19}	6	62.8768	0.079	3
	R(3,F$_1$)	3057.7607	1.260×10^{-19}	6	62.8757	0.079	3
$\nu_1 + \nu_4$	R^a(0,A$_1$)	4223.9053	2.353×10^{-21}	6	0	0.076	3
	R^a(1,F$_1$)	4229.1940	2.236×10^{-21}	6	10.4816	0.087	3
	R^a(2,F$_2$)	4234.3498	2.935×10^{-21}	6	31.4424	0.087	3
	R^a(2,E)	4234.4173	1.891×10^{-21}	6	31.4421	0.076	3
	R^a(3,A$_2$)	4239.2506	5.160×10^{-21}	6	62.8781	0.080	3
	R^a(3,F$_2$)	4239.4278	3.115×10^{-21}	6	62.8768	0.093	3
	R^a(3,F$_1$)	4239.5765	3.179×10^{-21}	5	62.8757	0.082	3
	Q^b(1,F$_1$)	4324.9331^g	1.307×10^{-21}	6	10.4816	0.078	3
	R^b(1,F$_1$)	4328.4319^g	7.519×10^{-23}	3	10.4816	0.081	3
	Q^b(3,F$_2$)	4330.6300^g	1.024×10^{-22}	6	62.8768	0.083	3
	R^b(0,A$_1$)	4333.6690^g	4.087×10^{-21}	6	0	0.091	3
	R^b(3,F$_1$)	4334.4357^g	6.777×10^{-23}	3	62.8757	0.079	3
$\nu_3 + \nu_4$	Q(2,F$_2$)	4330.1079^g	1.067×10^{-21}	6	31.4424	0.081	3
$2\nu_2 + \nu_4$	Q(4,F$_2$)	4332.2360^g	6.978×10^{-23}	3	104.7799	0.078	3
	Q(4,F$_1$)	4333.3108^g	1.000×10^{-22}	6	104.7746	0.079	3
$\nu_1 + \nu_2$	R(1,F$_1$)	4337.5489^g	1.082×10^{-21}	6	10.4816	0.77	3
$\nu_2 + \nu_3$	R(0,A$_1$)	4555.5645	5.226×10^{-22}	4	0	0.080	4
	R(1,F$_1$)	4566.9963	4.362×10^{-22}	4	10.4816	0.081	4
	R(2,F$_2$)	4578.6120	4.723×10^{-22}	4	31.4424	0.083	4
	R(2,E)	4578.6808	3.137×10^{-22}	4	31.4421	0.075	4
	R(3,A$_2$)	4590.2357	7.456×10^{-22}	4	62.8781	0.076	4
	R(3,F$_2$)	4590.4613	4.362×10^{-22}	4	62.8768	0.083	4
	R(3,F$_1$)	4590.6085	4.338×10^{-22}	4	62.8757	0.081	4

^{a}Rotational branch (br.), J and symmetry (E, A$_{1,2}$ or F$_{1,2}$) of the lower state, the index letters "a" and "b" allow for distinguishing between lines with the same indicated quantum numbers. ^{b}Line center. ^{c}Line strength (T_{ref} = 296 K). ^{d}HITRAN code for relative uncertainty: 3 ($\geq$20%); 4 ($\geq$10 and $\leq$20%); 5 ($\geq$5 and $\leq$10%); 6 ($\geq$2 and $\leq$5%). ^{e}Energy of the lower state. ^{f}Self-broadening coefficient. ^{g}Transitions used in HRS.

$$S_{\eta\eta'}(T) = S_{\eta\eta'}(T_{ref}) \cdot \frac{Q(T_{ref})}{Q(T)} \cdot \frac{\exp[-E_\eta/kT]}{\exp[-E_\eta/kT_{ref}]} \cdot$$

$$\frac{1 - \exp[-c_2 \times \tilde{\nu}_{\eta\eta'}/T]}{1 - \exp[-c_2 \times \tilde{\nu}_{\eta\eta'}/T_{ref}]} \tag{4}$$

where $S_{\eta\eta'}(T_{ref})$ is the tabulated line strength at the reference temperature (296 K) and E_η is the energy of the initial state (given in cm^{-1}). The total internal partition function Q runs through all allowed rovibrational states i, including the vibrationally fundamental and excited states

$$Q(T) = \sum_i g_i \exp[-E_i/kT] \tag{5}$$

with g_i the degeneracy of the level i. Due to its internal structure, having four half-integer spin hydrogen atoms at equivalent positions, the main isotopologue of CH_4 exists in three possible nuclear spin (NS) configurations differing in the value of the total nuclear spin (0/1/2 for para/ortho/meta isomers with spin symmetries E/F$_2$/A$_1$ respectively).[9]

Assuming there is no NS conversion, the para, ortho, and meta isomers constitute three independent species and have their own partition functions $Q_p(T)$, $Q_o(T)$, and $Q_m(T)$. Their relative populations remain constant and are defined by the initial conditions in which the gas is stored before being

processed. In our experiments, gas was stored at 300 K and the statistical weight between the nuclear spin isomers at this temperature is 2/9/5, for para/ortho/meta, respectively. This is an important phenomenon to consider, especially at low temperatures. As some of the lowest rotational levels are forbidden for some NS isomers (e.g., J = 0 of the vibrational ground state is allowed only for the meta isomer),[9] this will impact the dependence of $S_{\eta\eta'}(T)$ differently for each NS isomer, especially at low temperatures where the lowest J levels dominate the rotational distribution.

In the opposite case, assuming NS conversion, all three NS species can be considered as a single ensemble with a single $Q(T) = Q_p(T) + Q_o(T) + Q_m(T)$. The principle and details of the calculation on the relative line absorbance of the different nuclear spin species in the two cases (NS conversion or NS conservation) for CH_4 can be found in ref 17. Considering the temperature range addressed by this study (down to 40 K), we find a maximum relative difference of the partition functions between the two cases of around 2%. This value is beyond the accuracy of our model based on the HITRAN2016 line intensities S (with best precision S_{err} in the 2−5% range, see Table 1); therefore, throughout the text, the effect of NS dynamics is omitted. For more details on the values of different terms in the equations or their relations to the internal

molecular structure (e.g., dipole moments), see the appendix of ref 19 or the HITRAN online database.[20]

Finally, by applying the aforementioned relations, the p and T values can be retrieved by optimizing eq 1 to obtain the best possible match with $A_{exp}(\tilde{\nu})$. In the experiments described here, however, we do not measure $A(\tilde{\nu})$ directly. The transmitted signal is detected as power per unit area — intensity $I(\tilde{\nu})$. The Napierian absorbance is then retrieved by applying the Beer−Lambert law: $A(\tilde{\nu}) = \ln(I_0/I)$, where $I_0(\tilde{\nu})$ is the light intensity before the interaction.

A standard approach to find the optimal model, composed of individual components corresponding to observed transitions $\tilde{\nu}_{\eta\eta'}$ (eq 1), is to minimize the χ^2 function on the digitized data points $\tilde{\nu}_i$

$$\chi^2 = \sum_i w(\tilde{\nu}_i)\left\{A(\tilde{\nu}_i) - \sum_{\forall(\eta' \leftarrow \eta)}[\Phi_{\eta\eta'}\cdot\phi_{Voigt}(\tilde{\nu}_i - \tilde{\nu}_{\eta\eta'})]\right\}^2 \quad (6)$$

where $w(\tilde{\nu}_i)$ is the weight for given spectral point i, usually equal to the inverse of the square of its standard deviation. Also, for practical reasons, the integrated transition intensity $\Phi_{\eta\eta'} = n\cdot S_{\eta\eta'}$ is fitted rather than the pressure of the substance. Applying eqs 2 and 3 to define the surface-normalized Voigt line shape $\phi_{Voigt}(\tilde{\nu}_i - \tilde{\nu}_{\eta\eta'})$ only three quantities remain indetermined and are varied in the fit: the baseline function I_0, the temperature T, and the aforementioned transition intensity $\Phi_{\eta\eta'}$. After the convergence is achieved, the pressure corresponding to the intensity of transition $(\eta' \leftarrow \eta)$ is calculated using the gas law and eq 4

$$p_{\eta\eta'} = \frac{kT}{L}\frac{\Phi_{\eta\eta'}}{S_{\eta\eta'}(T_{ref})}\cdot\frac{Q(T)}{Q(T_{ref})}\exp\left[-E_\eta\left(\frac{1}{kT_{ref}} - \frac{1}{kT}\right)\right] \quad (7)$$

In an ideal case, the shape of the detected intensity would be driven only by the absorption of the substance under study. However, in many cases, the detection scheme itself could also influence the result. When this happens, the recorded I_{exp} is a convolution of the apparatus function F_{app} and the original transmitted signal I ($I_{exp} = I \times F_{app}$). This poses an additional problem because, in a general case, F_{app} does not commute with the Beer−Lambert transformation. Thus, additional processing of the signal must be applied before treating the spectra. This was also the case in our work where each of the experiments suffered from a different type of instrumental function distortion. As they are both different and closely related to the experiment, the details of the treatments are provided in the corresponding sections where the retrieval of p and T from the spectra is discussed.

■ EXPERIMENTAL SECTION

The spectral regions targeted by the two experimental setups are shown in Figure 1, whereas the list of selected transitions for analysis is presented in Table 1. In both setups, whose schematic outlines are given in Figure 2, CH_4 with a natural abundance of isotopologues and 99.9995% purity was used (N55, Air Liquide). The target for the LRS was to focus on the optimum accuracy and absolute precision in the higher temperature range to provide reference measurements. To this end, a relatively simple optical layout was used to minimize the measurement uncertainties that can arise when using a more complex layout, like the Herriott cell in the HRS case.
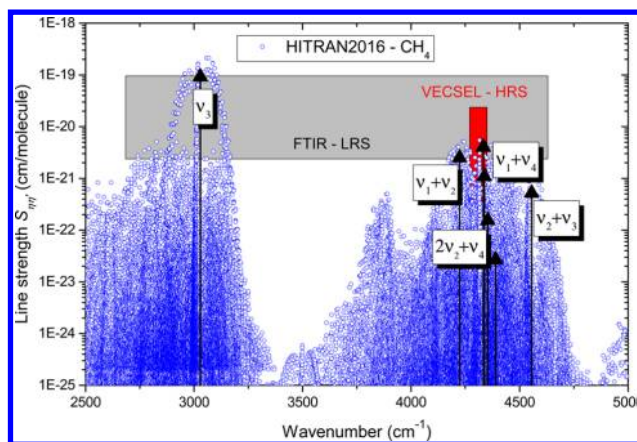

Figure 1. Methane line transition strengths $S_{\eta\eta'}$ according to the HITRAN2016 database.[18] The arrows point to the lowest J transitions of the bands used in this work.
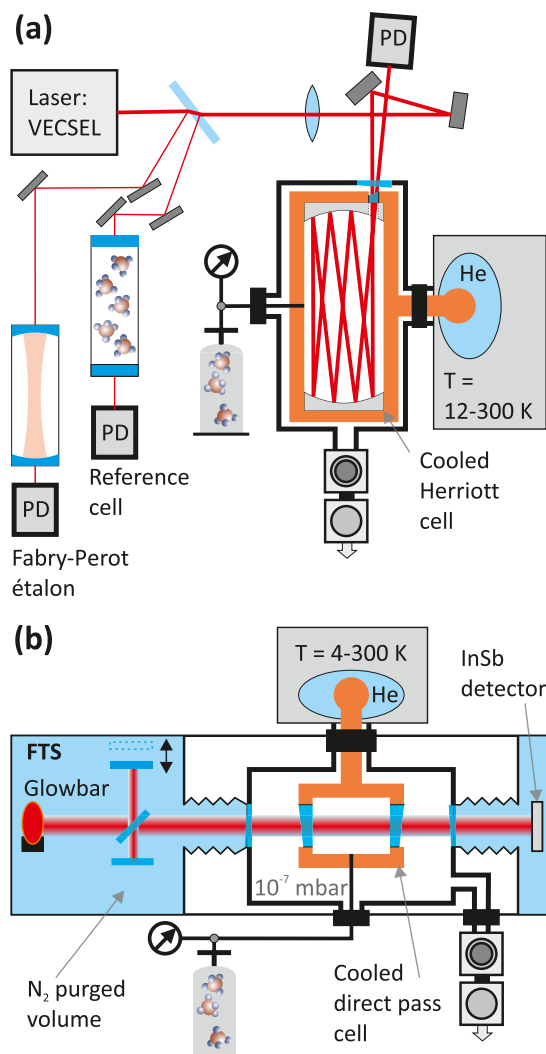

Figure 2. Experimental setups: (a) the high-resolution setup (HRS) and (b) the low-resolution setup (LRS). PD = photodiode.

Here, the aim was to exploit a long path length system and for the high spectral resolution and fast mode-hop-free scanning properties of the VECSEL to push the sensitivity limits to the lowest temperature limit. Combining the two datasets, we were

able to provide a coherent and accurate pressure analysis of methane at its solid- and gas-phase equilibrium across the whole temperature range studied, 40−77 K.

Low-Resolution Setup Description. In the LRS, absorption spectra were recorded in the 1600−4500 cm^{-1} spectral range using a Bruker IFS66 FTIR spectrometer. We used two wide range spectral sources: a halogen lamp for the near-IR range and a SiC Globar lamp for the mid-IR range, coupled to an infrared mercury−cadmium−telluride detector cooled with liquid nitrogen. To avoid a residual signal from the remaining atmospheric methane, the spectrometer and the volumes located on the line of sight were purged with pure N_2 (ALPHAGAZ 2, Air Liquide).

The direct path optical cell was initially designed for adsorption isotherm measurements.[21] The copper cell was equipped with two sapphire windows forming an optical path of length L_{LRS} = 1.746 ± 0.035 cm through the gas sample at thermal equilibrium (the description of the precise path length determination is presented in the Appendix). The cell was placed inside a cryostat equipped with KBr windows, continuously maintained under a vacuum of 10^{-7} mbar and cooled by a CTI-Cryogenics model 22 closed-cycle helium cryocooler. The cell temperature was regulated using a heater and a Lake Shore controller connected to a silicon diode (Lake Shore Cryogenics, model DT-500) fixed on the cell. The cell temperature was adjusted between 40 and 300 K with a precision of 0.1 K. The cell was connected to a stainless steel vessel at ambient temperature where the equilibrium pressures were measured in the range 10^{-4}−10 mbar using two MKS Baratron pressure gauges (0−1 and 0−10 mbar capacitive gauges with accuracy of 0.25% ± 0.0001 mbar and of 0.25% ± 0.001 mbar, respectively).

To prepare the solid−gas mixture for the Clapeyron curve measurements, roughly 3 mmol methane was introduced at 100 K (corresponding to 100 Torr in the cryogenic cell and ambient vessel). The cell was then cooled down to 45 K. At each fixed temperature between 45 and 80 K, the (p, T) and the corresponding IR spectra were collected at thermodynamic equilibrium. For each spectrum, 250−500 scans were recorded and averaged. In between measurements, the vessel maintained at ambient temperature was pumped to 10^{-7} mbar to avoid the contribution of molecules outgassing from the stainless steel walls.

After the measurement, the spectra were extracted from the recorded interferograms. To concentrate spectral information around the central lobe of the transition line, a common and standard procedure, named apodization, was applied. It consists of multiplying the interferogram by a selected mathematical function. The effect is to obtain a cleaner spectrum, useful when the density of lines is high but at the expense of the resolution R_S. In our case, the apodization function was set to the standard three-term Blackman−Harris function (BH3).[22] The resulting value of R_S = 0.13 cm^{-1} was then determined experimentally by measuring the width of isolated R(0,A$_1$) and R(1,F$_1$) transitions. Also, before extracting spectra from the interferogram, the spike associated with the reflections on the nonwedged windows of the sample cell was replaced by a flat line (see the blue curve in Figure 3). A detailed description of the numerical process applied to our FTIR spectra is described in ref 23.

The resulting transmittance spectra, together with the absorptance signal $\alpha_{P,exp} = 1 - I_{exp}/I_0$, for the lowest components of the rovibrational P, Q, and R branches are
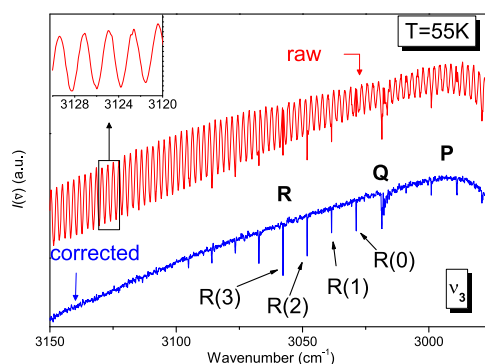

Figure 3. Effect of the interferogram correction on spectra recorded with the low-resolution setup, in the ν_3 asymmetric stretching vibrational band. The interferences due to the use of nonwedged windows create a spike in the interferogram and give rise to oscillations on the raw spectrum. Replacing this spike by a straight line suppresses oscillations and gives the corrected spectrum with smooth baseline after Fourier transform (shifted in intensity on the figure, for clarity).

shown in Figure 4. The absorptance $\alpha_P(\tilde{\nu})$ was preferred before the absorbance $A(\tilde{\nu})$ for two reasons. First, it is a recommended quantity to account for the effects inherent to the Fourier transform spectra (FTS),[24,25] and second, it allows a better graphical comparison of the spectra. Note, that in the case of small absorption $I \approx I_0$, the α_P converges toward A/L.

The main target for the FTIR analysis was to record the rovibrational lines in the ν_3 asymmetric stretching vibrational CH$_4$ band around 3048 cm^{-1} (Figure 4b). Lines from the $\nu_1 + \nu_4$ band were used to obtain a better signal at higher temperatures (Figure 4c), whereas the lines from the $\nu_2 + \nu_3$ band were used for the precise measurement of the L_{LRS} (see Appendix). The baseline noise, estimated from the root mean square of the fully transmitted signal, was approximately 0.002, comparable to that of the HRS. However, due to the much smaller optical path, the minimum detectable absorption coefficient $(A_{exp}(\tilde{\nu})/L)_{min}$ was only around 1×10^{-3} cm^{-1}.

High-Resolution Setup Description. The VECSEL source, used in the HRS, was a custom developed device based on the unit described in detail in ref 26. The optically pumped semiconductor core containing the active medium on top of a Bragg mirror was provided by IES Montpellier.[27] The 0.33 mm long external cavity was formed by a highly reflective spherical mirror of 2 mm radius placed on a tubular piezotransducer. It produced a single mode continuous emission with a narrow line width below 3 MHz on a 1 ms timescale. Variation of substrate temperature allowed VECSEL to cover the spectral range between 4270 and 4340 cm^{-1}. The continuous and mode-hop-free tuning of up to 15 cm^{-1} was performed by the external cavity piezodriven scans.

The light from the VECSEL was coupled into the L_{HRS} = 692 ± 5 cm path length Herriott cell (HC) and then analyzed by a photodiode (type G8423 from Hamamatsu coupled with a homemade transimpedance amplifier with a bandwidth of 0.6 MHz). The details of the HC design can be found in ref 16, and the precise L_{HRS} determination, in ref 17. A part of the main beam was also diverted to a Fabry−Pérot (FP) étalon (with a free spectral range, ∼0.0242 cm^{-1}) and to a reference cell filled with methane at low pressure (40 cm long and about 10 mbar of CH$_4$) to provide a signal for precise frequency calibration (with a precision better than 0.001 cm^{-1}).
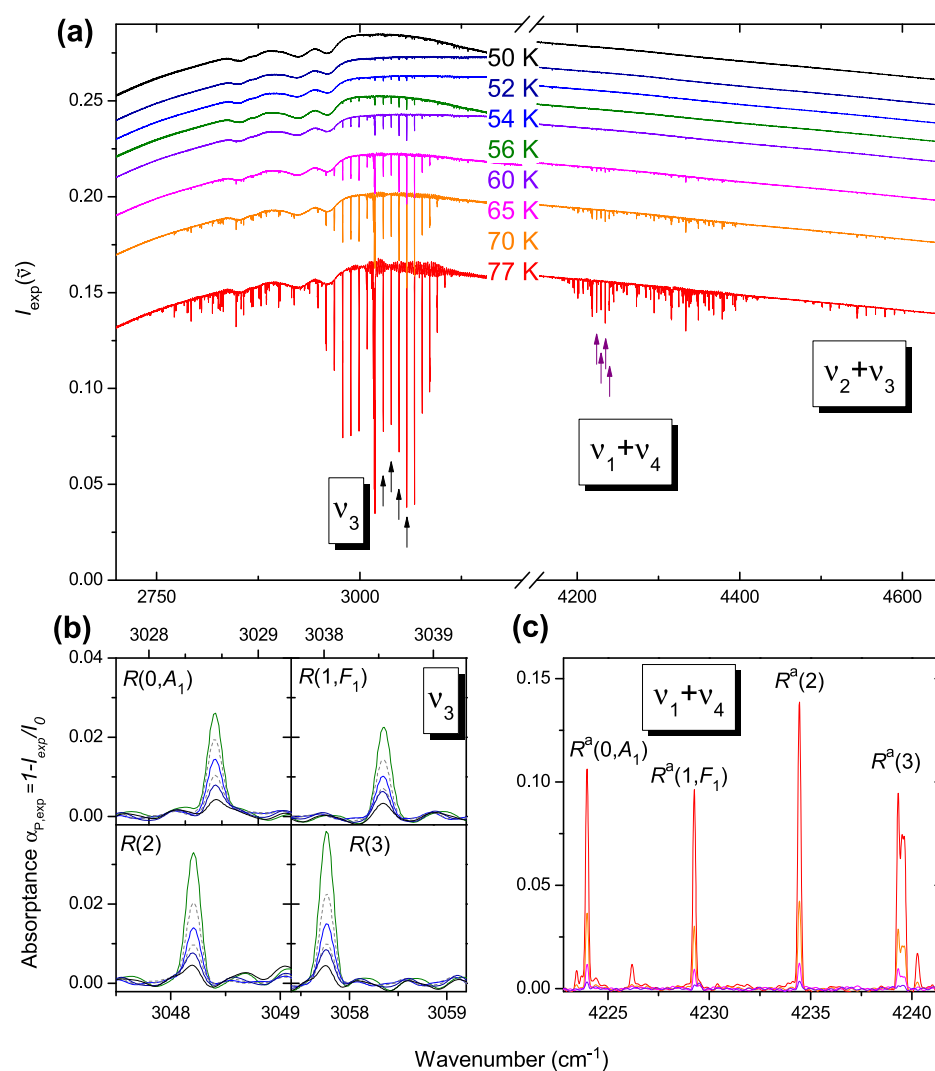
Figure 4. Absorption spectra of methane in the spectral region of the ν_3 and $\nu_1 + \nu_4$ vibrational bands recorded at different temperatures using the LRS. (a) Evolution of recorded light intensity, $I(\tilde{\nu})$, with temperature. Spectra have been shifted vertically from each other for clarity. The transitions used in the analysis are indicated by red and pink arrows for the lowest and higher temperature range, respectively. The evolution of the absorptance $\alpha_P = 1 - I/I_0$, for selected rovibrational transitions in the ν_3 band (b) and in the $\nu_1 + \nu_4$ band (c) is shown in detail on the lower plots.

The HC temperature was stabilized to absolute variations below 0.1 K using the Lake Shore Cryogenics model 331 temperature controller. Cryogenic cooling was supplied by the CTI-Cryogenics model 22C Cryodyne cooler, and two 25 Ω resistors were used for the heating. The temperature was measured with two calibrated silicon diodes, Lake Shore Cryogenics model DT-670 with calibration accuracy ±0.25 K between 30 and 60 K and ±0.15 K between 60 and 300 K.[16] One of the probes, T_A, was placed close to the "cold finger" cooler and was used as a reference for the temperature-locking circuit. The second, T_B, was located on the cell far from the heating resistors, to provide an independent measurement of the actual temperature. The difference between T_A and T_B varied from 0.12 to 0.20 K for the series of measurements performed, in which the temperature was decreased slowly from 70 to 40 K. The importance of this temperature measurement will be discussed later. For sample manipulation and pressure measurements (performed by the 0−10 mbar Pfeiffer CMR capacitive gauge with a precision of 0.001 mbar), the HC was connected to a vacuum system (at room temperature) through a 6 mm inner diameter steel pipe.

Detailed descriptions of the VECSEL, the Herriott cell, and the calibration process can be also found in a previous study performed with the HRS.[28]

To probe the entire rotational population of the lowest levels ($J = 0−4$) of combination bands of different vibrational modes (Table 1), we performed scans about 12 cm⁻¹ wide centered around 4330 cm⁻¹. The repetition rate of the scans was limited by the rapidity of the amplified photodiode detector. On the other hand, a high recording speed was beneficial in reducing the effects of mechanical noise in the system (caused by both the cryogenic cooling system and the vacuum pumps). As a compromise, we set the tuning speed to around 18 THz s⁻¹, corresponding to a 50 Hz spectral acquisition repetition rate.

At the beginning of the Clapeyron curve measurements, the HC was pumped down to 10⁻⁵ mbar and was then filled with around 9 mbar of methane at 77 K. Filling was stopped once the absorption signal stabilized, i.e., once the saturated vapor pressure was reached. The gaseous sample was then cooled progressively (~4 h) down to 40 K (when the absorption signal disappeared in the baseline noise) with intermediate
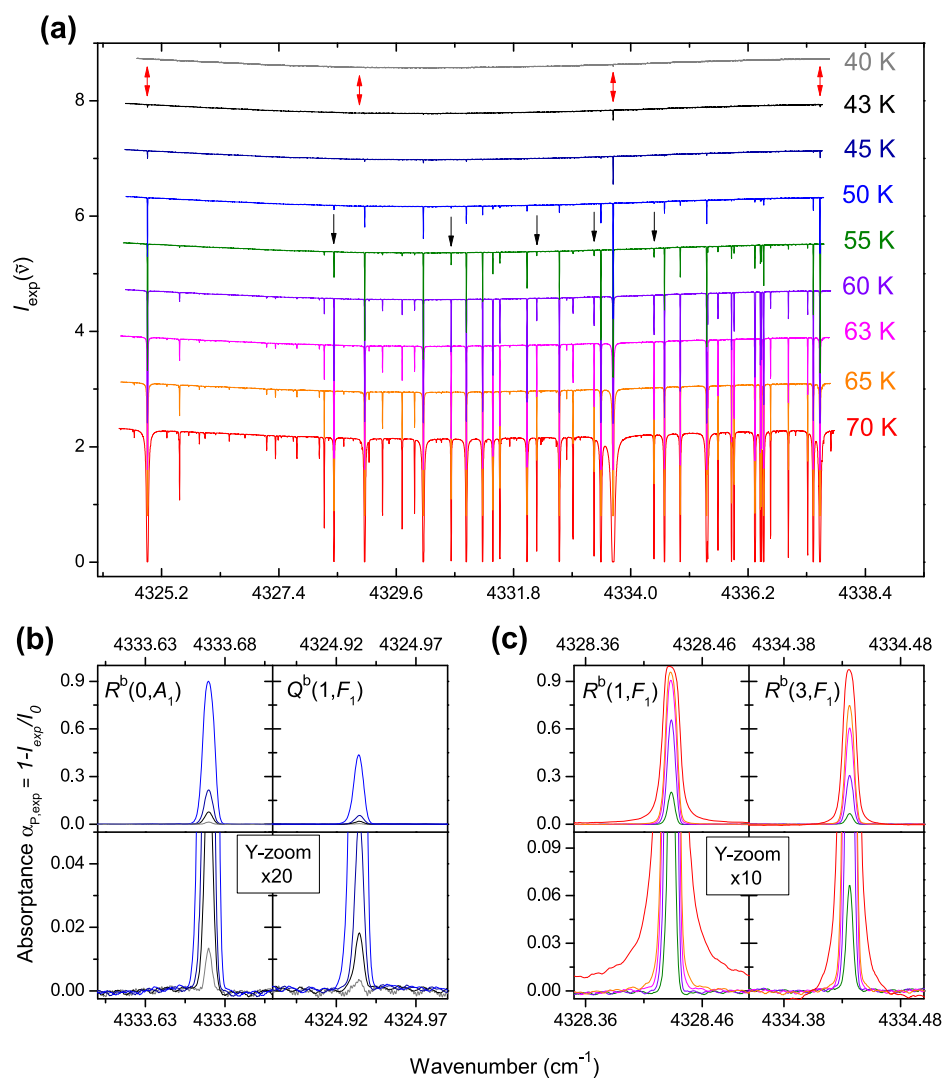
Figure 5. Absorption spectra of methane in the spectral range around 4330 cm^{-1} recorded with the HRS. The intensity of light, $I(\tilde{\nu})$, recorded at different temperatures, is shifted vertically for clarity (a). Red and black arrows correspond to the rovibrational transitions used at lower and higher temperatures, respectively. (b) and (c) show the absorptance signal for an example of two transitions from each group.

temperature plateaus of a few minutes duration to record corresponding IR spectra. For each temperature, 32 scans were recorded, calibrated, and averaged (Figure 5a). Figure 5b,c shows a part of the absorptance corresponding to a couple of transitions used in the analysis. The baseline noise, estimated from the root mean square of the fully transmitted signal was approximately 0.001, leading to a minimum detectable absorption coefficient $(A_{exp}(\tilde{\nu})/L)_{min}$ of about 1.4×10^{-6} cm^{-1}.

ANALYSIS OF THE VAPOR PRESSURE CURVE

In the first part of this section, we discuss the procedure used to retrieve the p and T values from the LRS and HRS experimental spectra. In the second part, we deal with the thermodynamic interpretations of the results and their comparison with previously published data.

Retrieval of p and T from the Spectra. An important point to discuss before dealing with the treatment of the absorption spectra at temperatures below the freezing point is the influence of solid-phase absorption. In the case of methane, this is a well-known phenomenon. For example, a detailed spectroscopic study covering both the temperature and spectral

ranges of our work was performed by Grundy et al.[29] Above 20 K, methane is in its crystalline phase I, in which the absorption peaks are tens of nanometers broad.[30] In our case (Figures 5a and 4a), this effect was observable only by a small decrease of the baseline level, with no impact on the retrieval process.

Due to differences in the apparatus function, two different approaches were used to treat the signals from the LRS and HRS experiments. The common point of the analysis was the application of the aforementioned methodology. This included the approximation of the absorption profile by the Voigt function. Although it is well known that it does not exactly reproduce the molecular transition profiles, neither the Hartmann–Tran profile (HTP), which is currently suggested by the IUPAC task group to model the molecular transition line shape,[31] nor any other "beyond Voigt" line shape models were used here, due to the fact that (i) our measurements were performed at low temperatures, where the Doppler broadening dominates the collisional one, and (ii) the uncertainty of $S_{\eta\eta'}$ (Table 1) in the range 2−5% was greater than the possible error of using the Voigt line shape model within the p and T values of this work.[32]
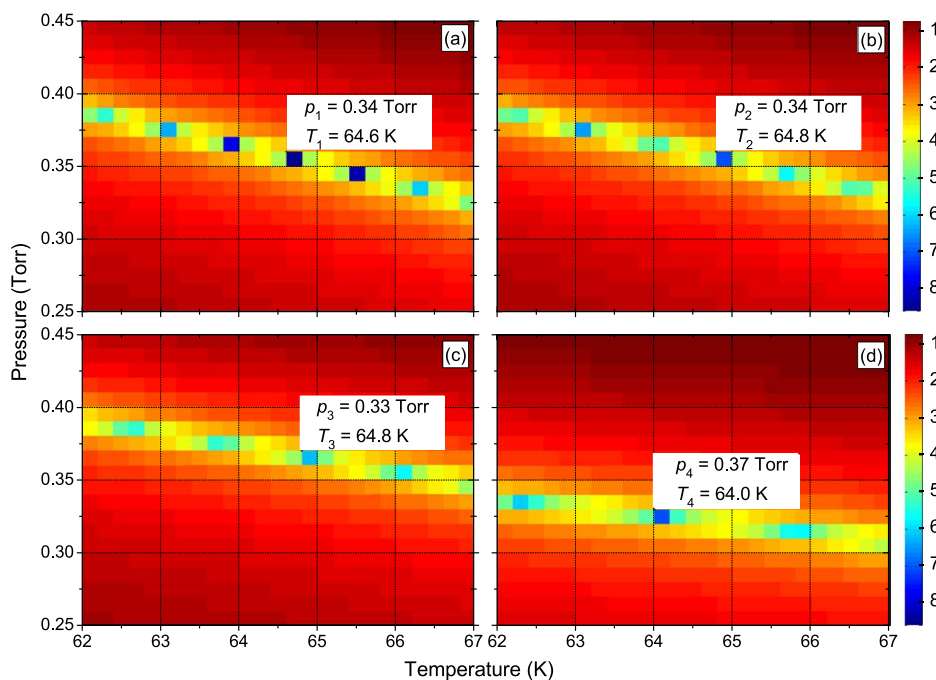
Figure 6. Example of a $\kappa^2(p,T)$ map for 65 K data recorded with the LRS. (a)–(d) represent, respectively, R(0), R(1), R(2), and R(3) lines of the $\nu_1 + \nu_4$ CH$_4$ vibrational band.

LRS. The first fact we had to consider before fitting the spectra was the role of the apparatus function F_{LRS}. Note that at 60 K, neglecting the collisional broadening, transitions in the 3000 cm^{-1} range have w_{Gauss} around 120 MHz or 0.004 cm^{-1} (eq 3). This is almost a 100 times less than the width of the instrument apparatus function (around 0.1 cm^{-1}, see the section Low-Resolution Setup Description). This means that the retrieved signal $I_{\mathrm{LRS}}(\tilde{\nu})$ is the convolution of the absorption $I_0 \exp[-A(\tilde{\nu})]$ with the apparatus function $F_{\mathrm{LRS}}(\tilde{\nu})$. Trying to extract $A(\tilde{\nu})$ using first Beer–Lambert transformation $\ln(I_0/I(\tilde{\nu}))$ and then deconvoluting this by $F_{\mathrm{LRS}}(\tilde{\nu})$ is not strictly correct as the two operations do not commute.

In the case of Fourier transform spectra, a boxcar function was used to represent the F_{LRS}

$$F_{\mathrm{LRS}}(\tilde{\nu}) = 2/R \cdot \mathrm{sinc}(2\tilde{\nu}/R) \tag{8}$$

with R as the LRS resolution. As in FTIRs, the entrance intensity $I_0(\tilde{\nu})$ is generated by a light source that is spectrally broad compared with the width of the apparatus function; the convolution $I_0(\tilde{\nu}) \times F_{\mathrm{LRS}}(\tilde{\nu})$ leaves I_0 intact. Contrary to $A(\tilde{\nu})$, the resulting absorptance $\alpha_{\mathrm{P,exp}}$ is then directly proportional to the sample absorptance $\alpha_{\mathrm{P}}(\tilde{\nu})$

$$\alpha_{\mathrm{P,LRS}}(\tilde{\nu}) = \left[1 - \frac{I_0 - I_{\mathrm{LRS}}}{I_0} \right]$$
$$= \left[1 - \frac{(I_0 \times F_{\mathrm{LRS}}) - (I \times F_{\mathrm{LRS}})}{(I_0 \times F_{\mathrm{LRS}})} \right] \approx \alpha_{\mathrm{P}}(\tilde{\nu}) \times F_{\mathrm{LRS}} \tag{9}$$

In this case, the modified convergence criteria would be

$$\chi^2_{\alpha_{\mathrm{P}}} = \sum_{\forall \tilde{\nu}_i} w(\tilde{\nu}_i)[\alpha_{\mathrm{P,exp}}(\tilde{\nu}_i) - \alpha_{\mathrm{P,model}}(\tilde{\nu}_i)]^2 \tag{10}$$

There were two main reasons why we did not apply this procedure; instead, a modified criterion based solely on the amplitudes of the observed transitions $\alpha_{\mathrm{P,exp}}(\tilde{\nu}_{\eta\eta'})$ was used

$$\kappa^2(p, T) = \log_{10}\left\{ \frac{[\alpha_{\mathrm{P,exp}}(\tilde{\nu}_{\eta\eta'}) - \alpha_{\mathrm{P,model}}(\tilde{\nu}_{\eta\eta'})]^2}{\alpha_{\mathrm{P,model}}(\tilde{\nu}_{\eta\eta'})^2} \right\} \tag{11}$$

First, we had to take into account the low resolution of our LRS system hindering the physical line shape of the transitions. As a consequence, the only reliable information we can get from the spectra is the intensity of absorption peaks. Even more, this only stands for individual transitions like R(0,A$_1$). In cases like the R(2) line at 3048.2 cm^{-1}, the two ortho and para transitions are separated only by 0.016 cm^{-1} (Table 1) and further information about their relative intensities is necessary to retrieve their individual intensities from the LRS spectra. The second point to be considered was the intensity noise. Although the filtering of the interferogram removed the largest oscillation, the remaining interference patterns had a greater influence on the surface than the height of the absorption lines. Considering both the low signal-to-noise ratio and the low resolution of the system, the choice of the amplitude-based convergence criteria (eq 11) over the integrated absorptance one (eq 10) was justified.

To further simplify the situation, the transitions for analysis were selected in such a way that they could be treated individually in a narrow spectral region surrounding the line. For $T < 56$ K, the rovibrational lines of the ν_3 band around 3100 cm^{-1} were used, whereas for temperatures between 56 and 75 K, the lines associated with the $\nu_1 + \nu_4$ (4230 cm^{-1}) band were used. At higher temperatures, only the lines related to the $\nu_2 + \nu_3$ band located around 4550 cm^{-1} were not saturated. This is the reason why these lines were used for calibrating the length of the cell, as already mentioned. Selecting a single line per range allowed considering the baseline I_0 as a constant, leaving only two free parameters per fit interval—p and T (see the Methodology section and the discussion following eq 6). The benefit of this approach was to limit the effect of the uncertainty in the line position as, with only a single line in the range, the spectrum could be shifted to

Table 2. Temperature/Saturated Pressure from Low-Resolution Setup Spectra

				LRS			
T_{spec} (K)	δT_{spec} (K)	$T_{diode}{}^a$ (K)	δT_{diode} (K)	p_{spec} (Pa)	δp_{spec} (Pa)	$\ln(p_{spec})$	$\delta p_{spec}/p_{spec}$
51.9	1.1	50.141	0.5	0.467	0.093	−0.762	0.200
51.8	1.8	53.141	0.5	0.813	0.067	−0.207	0.082
52.2	1.6	54.141	0.5	1.307	0.133	0.267	0.102
52.8	1.4	55.141	0.5	2.266	0.133	0.818	0.059
58.5	1.3	59.141	0.5	9.999	0.667	2.303	0.067
64.4	0.4	64.141	0.5	46.663	2.666	3.843	0.057
69.1	1.7	69.141	0.5	199.983	13.999	5.299	0.070
76.6	1.4	76.141	0.5	933.254	53.329	6.839	0.057

^{a}Temperature from the diode sensor.

match the experimental line center to the HITRAN2016 $\tilde{\nu}_0$ value (Table 1). Small exceptions were the components of R(2) and R(3) transitions in the case of LRS, which were blended due to the apparatus function and formed a single peak, and therefore, in fact, the same process could have been applied.

In practice, to find the global minimum of eq 11 for every selected transition $\{i\}$, we generated simulations on a grid of (p, T) coordinates (Figure 6). The values measured by the temperature sensor and the pressure gauge were used to produce a first estimate of the central values of the grid and the ranges for the T and p variations. The same value of the variation step $\Delta T = 0.2$ K was used for the temperature. In the case of the pressure step, Δp was chosen so that the $\Delta p/p$ was in the range ~1−10%. For each selected range, we determined the p_i and T_i values as those corresponding to a simulation with the minimal value of the $\kappa_i^2(p,T)$ quantity (eq 11). The error in the p_{spec} and T_{spec} values reported in Table 2 was obtained by measuring the dispersion of the p_i and T_i from the different rovibrational lines. In Figure 6, the variation of the κ_i^2 parameter with p and T is mapped for the $R^a(0,A_1)$, $R^a(1,F_1)$, $R^a(2,F_2,E)$, and $R^a(3,A_2,F_1,F_2)$ lines of the $\nu_1 + \nu_4$ band recorded around 65 K.

It is convenient to introduce dimensionless parameters $\Pi = p/p_{TP}$ and $\theta = T/T_{TP}$, where $p_{TP} = (116.96 \pm 0.02) \times 10^{-2}$ Pa and $T_{TP} = 90.6941 \pm 0.0025$ K are the pressure and the temperature at the triple point. Anticipating the dependence of the saturated pressure described by the Clapeyron curve, $\ln(\Pi)$ function of $(1/\theta - 1)$ is a curve that crosses $(0, 0)$ value and is a straight line if enthalpy of sublimation is strictly constant under the triple point. For this reason, Figure 7 represents $\ln(\Pi)$ as a function of $(1/\theta - 1)$ for LRS data. As the temperature varies from 40 to 77 K, θ varies from 0.44 to 0.85 and $1/\theta - 1$ from 1.27 to 0.17. The formula given by Armstrong $\log_{10}(p/\text{Torr}) = 7.69540 - 532.20/(T/K + 1.842)$[12] is converted to (θ, Π) units and plotted in the figure. The two sets $\{T_{spec}, p_{spec}\}$ and $\{T_{diode}, p_{spec}\}$ are plotted with their corresponding uncertainties. The pressure measured by the gauge p_{gauge} is also presented down to 40 K and exhibits a progressive deviation, which is addressed as a transpiration effect.[7]

This effect is due to the fact that the pressure measurement of methane at low temperature T in the cryogenic cell is performed by a capacitive gauge at ambient temperature T_h connected to the cell by a narrow tube. The effect becomes important when the mean free path λ of gaseous molecules is of the order of the diameter of the connecting tube. In this case, the measured pressure p_h is different from the real pressure in the cell p. Figure 8 displays the p/p_h ratio in the
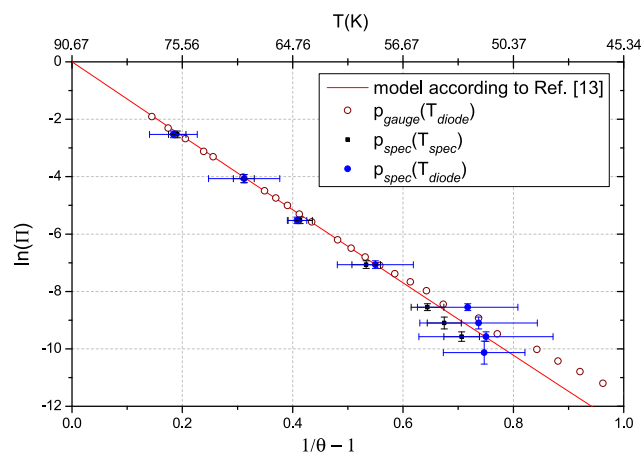

Figure 7. LRS data. Plain curve: Armstrong equation; purple dots: pressure from the gauge. The two sets $\{T_{spec}, p_{spec}\}$ and $\{T_{diode}, p_{spec}\}$ are plotted with a corresponding error bar that represents the uncertainty in the dimensionless $1/\theta$ and $\ln(\Pi)$ where $\Pi = p/p_{TP}$ and $\theta = T/T_{TP}$.
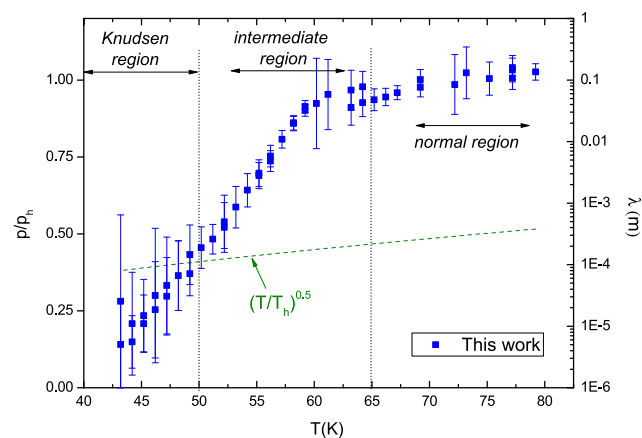

Figure 8. Transpiration effect, as measured in the LRS. The expected theoretical law $(T/T_h)^{1/2}$ valid below 50 K is represented by the dashed line.

case of the LRS, where the pressure p in the cell is calculated from Clapeyron's law. At 50 K, e.g., the pressure measured by the gauge is half of the real pressure. For $T > 65$ K, no transpiration effect occurs and the value is equal to 1. For $T < 50$ K, the p/p_h ratio roughly evolves as $(T/T_h)^{1/2}$ (Knudsen domain). For T between 50 and 65 K, the ratio evolves in an intermediate way, following an empirical law proposed by ref 33. Trying to determine new values for coefficients of a more

recent refined empirical law proposed in ref 7 was not possible in this work because the outgassing from the walls limits the methane pressure measurements.

HRS. Unlike in the FTS case, the combination of narrow VECSEL line width with its fast frequency tuning rate ensures that the spectra recorded by the HSR contain negligible broadening by the apparatus function. In that case, the absorbance $A_{HRS}(\tilde{\nu}) = A(\tilde{\nu})$ and the corresponding p and T values can be found by minimizing eq 6 and then using eq 7.

However, as seen in Figure 5, in our case, a small asymmetry was observed in the line profiles, which could affect the retrieval of the integrated area. Indeed, for strong lines, this effect is clearly visible, as can be observed in the example shown in Figure 9. The reason was determined to be that,
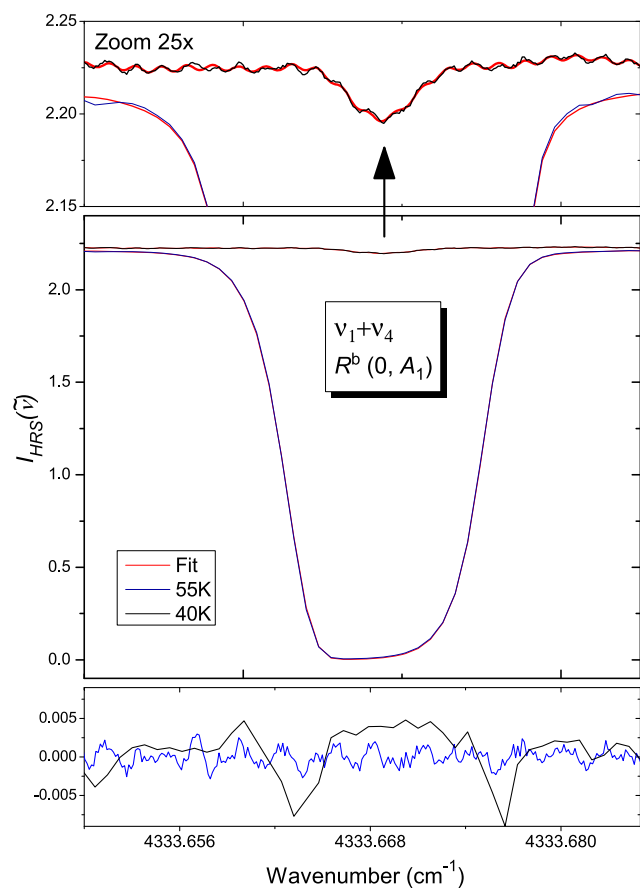

Figure 9. Example of HRS signal fit. The graph shows the fit and residuals for the $R^b(0,A_1)$ transition of $\nu_1 + \nu_4$ recorded at 40 and 55 K.

compared with previous experiments, the recorded spectral range was enlarged (to 12 cm^{-1} to record the same scan lines $Q^b(1,F_1)$ and $R(1,F_1)$ located at 4324.9331 and 4337.5489 cm^{-1}, respectively) while maintaining the same repetition rate. Consequently, the scanning speed was increased and the response time of the detector became visible. In this case, the convolution of the absorption spectrum with the apparatus function, which could be represented by an exponential decay (defined by the time constant τ), does not commute with the logarithm in the Beer−Lambert law. This leads to a systematic underestimation of the retrieved line intensities, in the case of strong peaks, when they are obtained by simply fitting the absorbance (eq 10). To correctly account for this effect, the

recorded signal must be fitted by the numerical representation of this convolution

$$\chi^2_{HRS} = \sum_{\forall \tilde{\nu}_i} w(\tilde{\nu}_i)$$

$$\{I_{HRS}(\tilde{\nu}(t_i)) - I_0 \exp[-A(\tilde{\nu}(t_i))] \exp[-\Delta t/\tau]\}^2 \tag{12}$$

Note that in this case, the convolution is in the temporal space, rather than in the spectral space like that for the LRS, due to the nature of the instrument effect. To this end, we have developed a dedicated fitting program that was used to treat all HRS signals with the time-decay constant deduced from the HRS detector bandwidth (1.7 μs). An example is given in Figure 9 where the fitting curve is drawn for the $R^b(0,A_1)$ transition recorded at 40 and 55 K. The residual curves confirm the correctness of the fit, for both "small" symmetric and "strong" asymmetric lines. A small excess of noise is visible at 55 K due to the fact that, in this region, where the signal nearly drops to the zero level (complete absorption), a lesser weight is used in the fit.

Considering the aforementioned issues, the selection of the transitions used for analysis were limited to those with a reasonable level of transmittance signal (approximately $A < 3$) to have the best possible estimation of surface. Due to the large temperature range addressed in the study, there was no transition that would fit this criterion across all measured spectra. Therefore, we had to create different selections for temperatures. $Q(1,F_1)$, $Q(2,F_2)$, $R^b(0,A_1)$, and $R(1,F_1)$ lines (see Table 1 for attribution) with $S_{\eta\eta'} > 10^{-21}$ cm mol^{-1} were used between 40 and 50 K (Figure 5b), whereas less intense $R^b(1,F_1)$, $Q(3,F_2)$, $Q(4,F_2)$, $Q(4,F_1)$, and $R^b(3,F_1)$ lines were preferred at higher temperatures (Figure 5c) up to 70 K. Unfortunately, for the three of them ($R^b(1,F_1)$, $Q(4,F_2)$, and $R^b(3,F_1)$), the accuracy of S is claimed to be above 20% (Table 1). In the treatment, their weights were reduced accordingly. For each temperature, up to four values of pressure were obtained and had to be averaged correctly. In such measurements, error analysis is crucial, and in our case, was done considering the factors present in eq 7. The relative error $\delta p/p$ was obtained by summing the contribution to L (0.8%), $A_{\eta\eta'}$ (given by the fit process from 1 to 10%), S (given by the error code in HITRAN, Table 1), and temperature T. For the evaluation of the temperature contribution, an absolute accuracy of 0.25 K (as mentioned in the experimental part) yields a relative error of 0.6% for the lowest temperature of 40 K; this propagates in eq 7 to less than 1%, including the three T-dependent terms present. The value of 0.25 K is discussed below because of the exponential dependence of the pressure with the temperature.

Figure 10a presents the data points corresponding to the nine transitions in a $(\ln(\Pi), 1/\theta - 1)$ plot, as defined above, compared with Armstrong's formula[12] converted to dimensionless Π and θ. In this case, the dynamical range of the variation of the saturated pressure does not allow us to clearly visualize the differences between the different data. Thus, two residuals are plotted on the lower panels: the difference with the pressure given by Armstrong's formula (Figure 10b) and the difference with a linear fit $\ln(\Pi)$ function of $(1/\theta - 1)$ (Figure 10c).

Although the error bars are wide compared with the dispersion of the data, it is clear that one data set is shifted. This corresponds to the $Q(4,F_2)$ transition located at
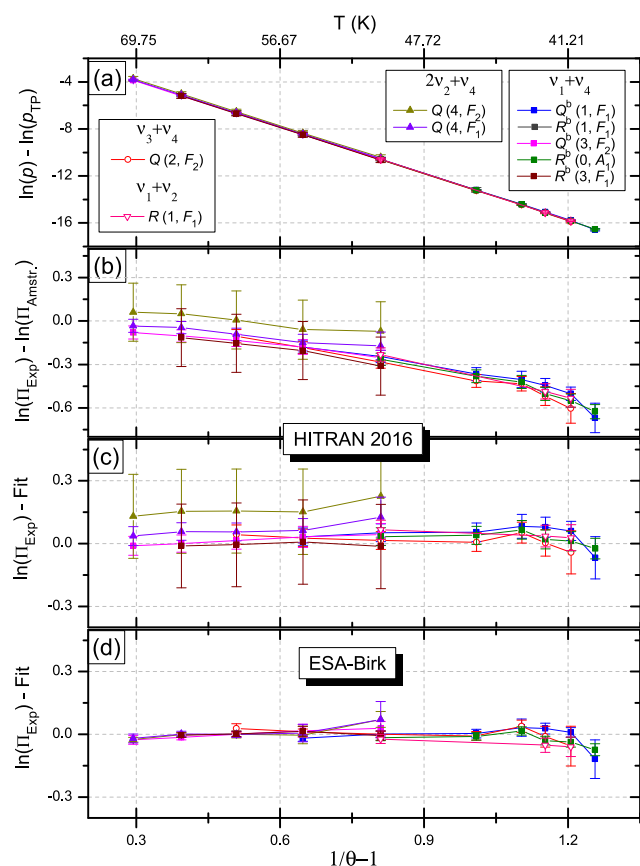
Figure 10. Upper panel (a): saturated pressure data points. The relative differences of saturated pressure, measured by the spectroscopy using the HITRAN2016 database, between Armstrong formula from ref 12 and the fitted linear curve are plotted in (b) and (c), respectively. (d) shows the relative differences between p retrieved using the ESA-Birk database and a fitted linear curve.

4333.2360 cm^{-1}. The value of $S_{\text{HITRAN2016}} = 6.978 \times 10^{-23}$ cm mol^{-1} appears to be too low, leading to an overestimation of the pressure. For this reason, different methane databases (experimental or theoretical) have been considered and compared to HITRAN2016: GEISA2016,[34] Theo296K,[35] EXOMOL,[36] Mecasda,[37] and ESA-Birk.[38] The more experimental ones (GEISA, ESA-Birk) give a value around 8.1×10^{-23} cm mol^{-1}. The relative difference of 16% remains within the accuracy of >20% assumed in HITRAN2016 but could be corrected.

The ESA-Birk database was developed for the atmospheric instrument TROPOMI and gives positions, intensities, and also air-broadening of molecular lines including HTP profile and line-mixing effects. The given uncertainty on the line strength is less than 0.5%. Fortunately, their range studied (4200–4340 cm^{-1}) covers that of our HRS data so it is straightforward to use this database rather than HITRAN2016. Confirmation was given within our experiment, where a reference spectrum of methane at room temperature was simultaneously recorded to calibrate each cold spectrum. It was possible to compare the two simulated spectra from the HITRAN2016 and ESA-Birk databases to our reference spectrum, and although minor discrepancies were observed with the first, the second spectrum almost perfectly matched the experimental data. Table 3 presents the comparison between the two databases for the nine transitions used in this study. The corrected datasets are shown as residuals in the lower panel of Figure 10d, where it can be observed that the major discrepancy has disappeared and the error bars have been reduced by 1 order of magnitude. Table 4 compares the pressures derived from the two databases including their uncertainties.

Clapeyron Curve. The measurement of the saturated pressure at temperatures below the triple point allowed us to consider the thermodynamics of sublimation and to determine its enthalpy for the methane molecule. The following paragraph recalls the basic aspects and tries to compare the results obtained by spectroscopy to previous determinations.

The boundary between two phases of a single (pure) substance is described by the Clapeyron equation

$$\frac{dp}{dT} = \frac{\Delta s}{\Delta v} \tag{13}$$

with Δs as the difference of molar entropies and Δv as the difference of molar volumes of the solid and gas phase.

Considering that our case is obviously far below the critical temperature, Δv can be approximated by the molar volume of the gas phase v_{g} for which the ideal gas law applies: $v_{\text{g}} = RT/p$, with $R = 8.3144598$ J mol^{-1} K^{-1} the molar gas constant. Accordingly, Δs can be characterized by the molar enthalpy of sublimation $\Delta_{\text{sub}}H$ as follows: $\Delta s = \Delta_{\text{sub}}H/T$ as, during phase change, temperature and pressure remain constant. Therefore

$$\frac{dp}{p} = \frac{\Delta_{\text{sub}}H}{R} \frac{dT}{T^2} \tag{14}$$

and, if the molar enthalpy of sublimation is considered as constant in the temperature range, the integration gives

$$\ln(p) = -\frac{\Delta_{\text{sub}}H}{R} \frac{1}{T} + \text{const} \tag{15}$$

Table 3. Comparison between HITRAN2016 and ESA-Birk Databases[a]

energy (cm^{-1})	label	E_η (cm^{-1})	$S_{\text{HITRAN2016}}$ (cm mol^{-1})	$S_{\text{ESA-Birk}}$ (cm mol^{-1})	Δ (%)
4324.9331	Q^b(1,F$_1$)	10.4816	1.307×10^{-21}	1.375×10^{-21}	4.9
4328.4319	R^b(1,F$_1$)	10.4816	7.519×10^{-23}	7.803×10^{-23}	3.6
4330.1079	Q(2,F$_2$)	31.4424	1.097×10^{-21}	1.113×10^{-21}	1.4
4330.6300	Q^b(3,F$_2$)	62.8768	1.024×10^{-22}	1.040×10^{-22}	1.5
4332.2360	Q(4,F$_2$)	104.7800	6.978×10^{-23}	8.155×10^{-23}	14.4
4333.3108	Q(4,F$_1$)	104.7747	1.000×10^{-23}	1.058×10^{-22}	5.5
4333.6690	R^b(0,A$_1$)	0	4.087×10^{-21}	4.295×10^{-21}	4.8
4334.4357	R^b(3,F$_1$)	62.8768	6.777×10^{-23}	6.727×10^{-23}	−0.7
4337.5489	R(1,F$_1$)	10.4816	1.041×10^{-21}	1.137×10^{-21}	8.4

^{a}E_η is the energy of the lower state of the transition, and the last column Δ is the relative difference in % for the two databases.

Table 4. Analysis of Pressure Values in HRS from the Two Databases

				HRS			
database		ESA-Birk			HITRAN2016		
T	δT	p	δp	$\delta p/p$	p	δp	$\delta p/p$
40.189	0.25	0.000727	1.3×10^{-5}	0.019	0.000764	3.4×10^{-5}	0.044
41.109	0.25	0.001496	4.0×10^{-5}	0.027	0.001575	7.8×10^{-5}	0.049
42.123	0.25	0.00300	7×10^{-5}	0.023	0.00320	0.00017	0.052
43.115	0.25	0.00598	6×10^{-5}	0.009	0.00630	0.00031	0.050
45.138	0.25	0.0202	0.0002	0.010	0.0212	0.0010	0.045
50.107	0.25	0.278	0.004	0.014	0.294	0.017	0.058
55.046	0.25	2.375	0.041	0.017	2.44	0.15	0.062
60.098	0.25	14.60	0.17	0.012	15.10	0.89	0.059
65.036	0.25	65.2	0.8	0.012	67.6	4.0	0.060
70.079	0.25	238.5	4.4	0.019	249.0	14.7	0.059

Table 5. Experimental Data Used for the Final Fit, Including Both LRS and HRS Data[a]

T (K)	$\theta = T/T_{TP}$	$\Pi = p/p_{TP}$	type	$x = (1/\theta - 1)$	δx	$y = \delta p/p$	$\delta y = \ln \Pi$	σ
40.18	0.443	6.22×10^{-8}	HRS	1.256	1.40×10^{-2}	−16.592	1.80×10^{-2}	0.19
41.10	0.453	1.28×10^{-7}	HRS	1.205	1.34×10^{-2}	−15.871	2.60×10^{-2}	0.18
42.12	0.464	2.56×10^{-7}	HRS	1.152	1.28×10^{-2}	−15.177	1.80×10^{-2}	0.17
43.11	0.475	5.11×10^{-7}	HRS	1.103	1.22×10^{-2}	−14.487	5.00×10^{-3}	0.16
45.14	0.498	1.72×10^{-6}	HRS	1.009	1.11×10^{-2}	−13.272	7.00×10^{-3}	0.15
50.10	0.552	2.37×10^{-5}	HRS	0.809	9.02×10^{-3}	−10.648	1.00×10^{-2}	0.12
55.05	0.607	2.03×10^{-4}	HRS	0.647	7.48×10^{-3}	−8.500	1.50×10^{-2}	0.10
60.10	0.663	1.24×10^{-3}	HRS	0.509	6.27×10^{-3}	−6.686	1.00×10^{-2}	0.08
65.03	0.717	5.58×10^{-3}	HRS	0.394	5.36×10^{-3}	−5.187	1.00×10^{-2}	0.07
70.08	0.773	2.04×10^{-2}	HRS	0.294	4.61×10^{-3}	−3.892	1.70×10^{-2}	0.06
53.13	0.586	6.95×10^{-5}	LRS	0.706	1.61×10^{-2}	−9.573	8.20×10^{-2}	0.23
54.14	0.597	1.11×10^{-4}	LRS	0.675	1.55×10^{-2}	−9.099	1.02×10^{-1}	0.23
55.14	0.608	1.93×10^{-4}	LRS	0.644	1.49×10^{-2}	−8.548	5.90×10^{-2}	0.20
59.13	0.652	8.54×10^{-4}	LRS	0.533	1.30×10^{-2}	−7.064	6.70×10^{-2}	0.18
64.14	0.707	3.99×10^{-3}	LRS	0.414	1.10×10^{-2}	−5.524	5.80×10^{-2}	0.16
69.14	0.762	1.71×10^{-2}	LRS	0.311	9.48×10^{-3}	−4.068	7.00×10^{-2}	0.14
76.14	0.839	7.98×10^{-2}	LRS	0.191	7.82×10^{-3}	−2.528	5.80×10^{-2}	0.12
90.69	1	1	TP	0	3.30×10^{-4}	0.000	5.00×10^{-3}	0.01

[a]The last column σ is the error including the linear fit uncertainties δy on y and δx on x, calculated by $\sigma^2 = \delta y^2 + a^2 \delta x^2$, where $a = -13.15 \pm 0.1$ is the slope of the straight line, $y = ax + b$. The values of TP: $T_{TP} = 90.6941 \pm 0.0025$ K and $p_{TP} = (116.96 \pm 0.02) \times 10^{-2}$ Pa were taken from ref 10.

which is the classical form of Clapeyron's law. If ΔH_{sub} is constant up to the triple point, its value is directly related to the slope of the straight line written with dimensionless parameters θ and Π

$$\ln(\Pi) = -\frac{\Delta H_{sub}}{RT_{PT}}\left(\frac{1}{\theta} - 1\right) \quad (16)$$

Indeed, as shown in Figure 7 for LRS and Figure 10a for HRS, the data points are nearly aligned on a straight line, and a preliminary value of the sublimation enthalpy can be estimated using eq 16. In fact, our datasets are limited to the range 40−77 K and eq 15 is preferred for a weighted fit on this limited temperature range $y = ax + b$ with $y = \ln(\Pi)$, $x = 1/\theta$, and a as the slope $\Delta H_{sub}/RT_{TP}$. To carefully evaluate uncertainties, it is important to consider the absolute accuracy of T in each setup and to propagate it on the pressure. So, the uncertainty σ_y to be regarded includes $\delta y = \delta\Pi/\Pi$, and that of the measurement of $x = 1/\theta$, $a\delta x = a\delta\theta/\theta^2$. The expression to be minimized is thus

$$\chi^2 = \sum \frac{(y - ax - b)^2}{\delta y^2 + (a\delta x)^2} \quad (17)$$

considering an error σ_y equal to $\sqrt{\delta y^2 + (a\delta x)^2}$. The data points are presented in Table 5, and the residuals are plotted in Figure 11. The result of the fit is a slope of $a = -13.15 \pm 0.10$ and an intercept of $b = 13.13 \pm 0.160$. With the value of $RT_{PT} = 753.872$ J, the molar enthalpy of sublimation is 9910 ± 75 J mol^{-1}.

Looking at Figure 11, we can conclude that the data points from the two independent experiments overlap well in the common temperature interval, confirming correct calibrations of the two experiments (mainly the optical path measurements). Second, considering the uncertainties of our measurements, it would be tempting to extrapolate the curve to the triple point. Putting $\theta = 1$ gives a pressure of $p = 11\,518(710)$ Pa, which is compatible with the value $p_{TP} = 11\,696(2)$ Pa. This extrapolation could suggest taking $\Delta_{sub}H$ constant in the whole 40−90.6941 K range and including the triple point in the data. However, this happens because of too large experimental uncertainties in the pressure and we will see in the next paragraph that a thermodynamical approach based on the measurement of heat capacity C_p for both gas and solid phases yields a small dependence of $\Delta_{sub}H$ with the temperature.
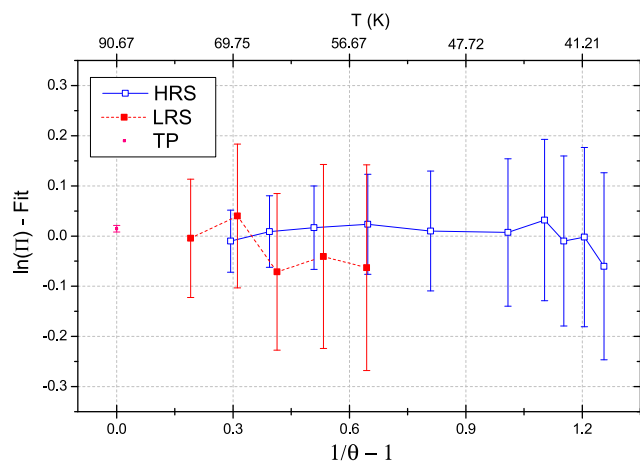
Figure 11. Residuals from the fit $\ln(\Pi)$ function of $(1/\theta - 1)$ on the whole range 40−90 K. The triple point is included in the fit with its uncertainties.

Thermodynamic Approach. The following equation expresses the enthalpy of sublimation at a temperature T below the triple point by

$$\Delta_{\text{sub}}H(T) = \Delta_{\text{sub}}H(T_{\text{TP}}) + \int_{T_{\text{TP}}}^{T} (C_{\text{pM}}^{\text{g}}(T) - C_{\text{pM}}^{\text{s}}(T))\, dT$$

$$(18)$$

where $C_{\text{pM}}^{\text{g}}(T)$ and $C_{\text{pM}}^{\text{s}}(T)$ are the isobaric molar heat capacities in the gas and solid phases, respectively, and $\Delta_{\text{sub}}H(T_{\text{TP}})$ is the molar enthalpy of sublimation at the triple point temperature T_{TP}. Its value is equal to the sum of the easily derived enthalpies of vaporization and fusion

$$\Delta_{\text{sub}}H(T_{\text{TP}}) = \Delta_{\text{vap}}H(T_{\text{TP}}) + \Delta_{\text{fus}}H(T_{\text{TP}})$$

$$(19)$$

The former value was calculated from a polynomial equation $\Delta_{\text{vap}}H(T) = f(T/T_{\text{TP}})$ containing four fitted parameters and is suitable for temperatures from the triple point to the critical point.[39] This value $\Delta_{\text{vap}}H(T_{\text{TP}}) = 8721$ J mol^{-1} is not far from $\Delta_{\text{vap}}H(T_{\text{TP}}) = 8731.29$ J mol^{-1} obtained by Setzmann and Wagner[10] using a more complete analysis of experimental data obtained between 60 and 3000 K. The enthalpy of fusion at the triple point is $\Delta_{\text{fus}}H(T_{\text{TP}}) = 928.4$ J mol^{-1}, determined by Colwell et al.[15] in the range 90.659−92.325 K. Here, $\Delta_{\text{sub}}H(T_{\text{TP}})$ will be taken to be 9659 ± 12 J mol^{-1}. Below the triple point, the value of $C_{\text{pM}}^{\text{g}}(T)$ was calculated from molecular properties.[40] A very small change is observed from 60 K ($4.0014 \times R$) to 90.6941 K ($4.0021 \times R$) very near to the value of $4R$ deduced from the kinetic theory. $C_{\text{pM}}^{\text{g}}(T)$ is taken at $4.0021 \times 8.3144598 = 33.275$ J K^{-1} mol^{-1}. Solid heat capacities were measured by Colwell et al. between 5 and 90.37 K. Taking into account that solid methane exists in two different solid phases, we considered only data in the temperature range of the present work, between 30 and 88.4 K, corresponding to the so-called phase I solid methane. To perform the integration of eq 18, it was useful to express $C_{\text{pM}}^{\text{g}}(T) - C_{\text{pM}}^{\text{s}}(T)$ as a polynomial formula. Hence it follows

$$C_{\text{pM}}^{\text{g}}(T) - C_{\text{pM}}^{\text{s}}(T)$$
$$= 34.2 - 1.20T + 1.40 \times 10^{-2}T^2 - 6.9 \times 10^{-5}T^3$$

$$(20)$$

The model reproduces the experimental data better than the experimental uncertainty estimated at 1%.[15] The measurement

at 90.4 K was not regarded in the fit, since it is too close to the triple point, for which a divergence of C_{pM}^{s} is produced because of the discontinuity of the entropy. To estimate how the 1% errors on C_{pM}^{s} are propagated to the enthalpy in the integration, two third-order polynomial formulae similar to eq 20 have been calculated with C_{p}^{s} increased or decreased by this amount. The uncertainty of 12 J mol^{-1} on $\Delta_{\text{sub}}H(T_{\text{TP}})$ in eq 18 was also included. Finally, the result is represented on Figure 12 by an uncertainty zone around the calculated
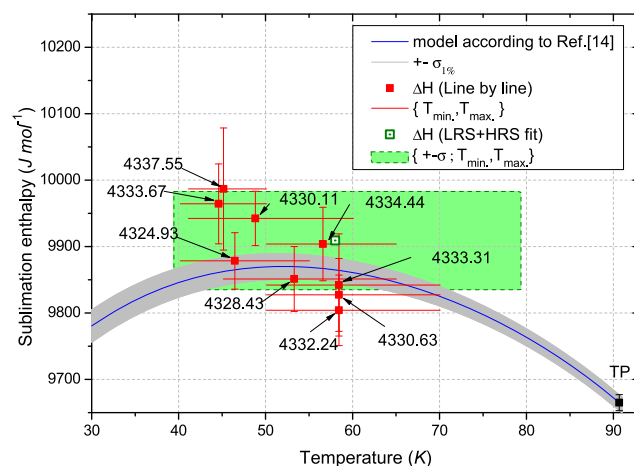

Figure 12. Variation of the sublimation enthalpy with temperature from 30 K to the triple point calculated from measured solid and gas heat capacities (eq 18) (blue curve) with 1% uncertainty (grayed zone). Our experimental values are represented by the red squares corresponding to the nine individual transitions, by the green rectangle derived from both LRS and HRS pressures. The vertical error bars are the $1 - \sigma$ uncertainty, and the horizontal extension concerned the temperature range.

enthalpy of sublimation $\Delta_{\text{sub}}H(T)$. The maximum of the curve is obtained at about 53 K ($\Delta_{\text{sub}}H(T) = 9870$ J mol^{-1}), and the variation of $\Delta_{\text{sub}}H(T)$ is less than 2% within the range of temperature 30−90.6941 K. Due to integration from the triple point (eq 18), the uncertainty increases as the temperature decreases, reaching a value of about 20 J mol^{-1} at 40 K. For comparison, in Figure 12, we plot a rectangle corresponding to our experimental determination $\Delta_{\text{sub}}H = 9910 \pm 75$ J mol^{-1} within our experimental range 40−77 K.

It can be observed that the difference between the experimental and calculated[15] $\Delta_{\text{sub}}H(T)$, both determined independently, is not significant. This becomes all the more evident if we consider that the uncertainties presented in the figure are of 1 standard deviation. The physical meaning of the experimental enthalpy of sublimation is thus confirmed and consequently the quality of experimental pressures and temperatures. However, their accuracy and, in particular, that of the absolute value of T is not yet high enough to observe a T-dependence of $\Delta_{\text{sub}}H(T)$, as proposed by the model given in (eqs 18 and 20), the dependence being very small as mentioned above. The required accuracy should be better than 1%. On the other hand, from the calculated curve, it is clear that the average of molar enthalpy in the 40−77 K range differs from the value at the triple point 9659 ± 12 J mol^{-1} by more than 1%. This confirms our reservations to include the triple point T_{TP}, p_{TP} in the data and to analyze them restricted to our studied temperature range.

Following this remark, considering the HRS setup, the relative uncertainty of the temperature measurement is clearly better than its absolute accuracy of 0.25 K. Then, eq 14 tells us that the enthalpy, slowly temperature dependent, can be considered as the derivative of the logarithm of the saturated pressure curve as a function of the inverse of the temperature. Thus, our measurements can be analyzed in a different way, focusing on the variation of the saturated pressure for a definite elevation of temperature (1 or 5 K in our case). In addition, each transition can be separately treated over a limited temperature range where its measurement is regarded confident. For our sets of transitions, we consider that enthalpy remains constant within each range, such a value being attributed to the middle of the range. In this process, the relative uncertainty on T is reduced to 0.03 K and the value of S does not interfere as it only goes in the intercept value of the linear fit of $\ln(p)$ as a function of $1/T$ (see eq 7). The results are reported in Figure 12 and show a small but not significant increase of enthalpy with decreasing temperature. Considering a constant value over the range 40−70 K, an average value including the nine transitions leads to the value 9885 ± 75 J mol^{-1}, practically an identical value to the one obtained from the linear fit of the average pressures (9910 ± 75 J mol^{-1}).

Finally, in Figure 13, we compare the saturated pressures derived from the thermodynamics (Colwell et al.[15]) with the
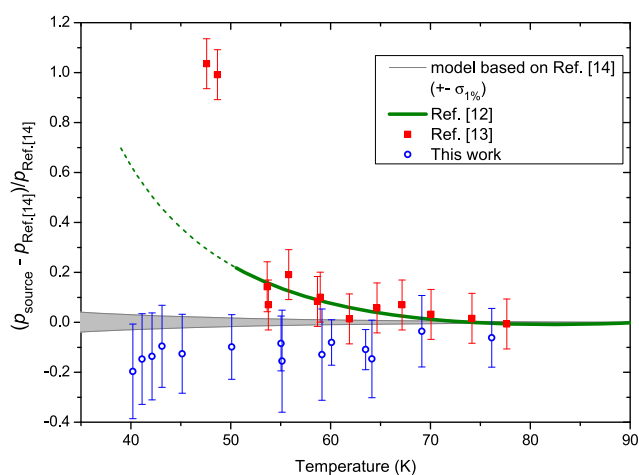

Figure 13. Comparison between the thermodynamic model derived from Colwell et al.[15] and experimental data for the saturated vapor pressure below the triple point. For clarity, the relative difference is plotted. Green curve: Armstrong's formula,[12] red squares: Tickner et al. data,[13] blue dots: our work.

experimental measurements of Tickner et al.,[13] the derived curve from Armstrong et al.,[12] and the present work. Let us note here that the pressure varies over 6 orders of magnitude

within the temperature range (and even 7 orders if the triple point is included). For clarity, the relative difference from the thermodynamic model is plotted. An uncertainty of 1% on the heat capacity measurement has been propagated in the pressure curve (gray zone) and gives an error of 3% at 40 K. Armstrong's curve shows a discrepancy of 18% at 54 K; Tickner's lowest points are 100% off around 50 K, but this was already mentioned in his paper; our data points lie from 18 to 5% lower in the range from 40 to 77 K.

■ DISCUSSION

In our experiment, the uncertainty, dominated by the absolute accuracy of the temperature (Figure 11), did not allow for the detection of a significant variation of the molar enthalpy of sublimation nor for a more refined computed curve,[41] as was done for water.[8] However, the retrieved value of $\Delta_{sub}H = 9910 \pm 75$ J mol^{-1} for the temperature range of 40−77 K was in agreement with the variation of ΔH_{sub} values calculated for the 30−90 K range from eq 18 (Figure 12).

To go further, it is important to improve the pressure measurement below 10^{-2} Pa as well as the absolute value of temperature. As demonstrated, spectroscopic measurement of the absorption of the gas is a good candidate for the first challenge. In principle, this can be done considering only one transition. As an example, the absorption of the $R^b(0,A_1)$ transition can be considered. Measurements in the 41−50 K range have an uncertainty better than 1%, which yields saturated pressure values given in Table 6 with a focus on the temperature T_B and T_A (temperature of the second sensor used for the servo-locking process). The choice of T_B was guided by the argument of an independent measurement with no coupling with electronics. However, here, T_A is also a temperature measurement at another point of the cell and less than T_B. Considering that saturated pressure is determined by the lowest temperature in the cell, it seems to be more appropriate to choose T_A instead of T_B. Do T_A or T_B really represents the real temperature of the gas? The difference $T_B - T_A$ varies from 0.081 K at 70 to 0.19 K at 40 K and influences by less than 1% the pressure derived from eq 7. However, for enthalpy determination, these pressure values have to be connected to a precise temperature. Using T_A instead of T_B in the treatment above including the nine transitions has been tested and led to a decrease in the enthalpy value of 1%, $\Delta_{sub}H = 9807(57)$ J mol^{-1} instead of 9885(75) J mol^{-1}. Let us recall that around 40 K, a variation of 7% on the pressure is observed for a temperature difference of 0.1 K and 90% for a gap of 1 K.

Therefore, the question of the temperature measurement must be posed. Instead of the contact sensors, there are two possible ways on our HRS setup to derive the temperature from the spectra. The first one is to consider the shape of each transition and to measure their Gaussian width driven by the

Table 6. Pressure Derived from Equation 7 for the Transition $R^b(0,A_1)$ Considering the Two Available Temperatures of the Cell in HRS, T_B and T_A

T_B (K)	T_A (K)	$p(T_B)$ (Pa)	$p(T_A)$ (Pa)	δp (Pa)	$\delta p/p$	$(p(T_B) - p(T_A))/p$
40.189	39.996	7.32×10^{-4}	7.24×10^{-4}	1.33×10^{-5}	0.018	−0.011
41.109	40.947	1.47×10^{-3}	1.46×10^{-3}	1.23×10^{-5}	0.008	−0.009
42.123	41.963	2.98×10^{-3}	2.96×10^{-3}	1.61×10^{-5}	0.005	−0.009
43.115	42.969	5.99×10^{-3}	5.95×10^{-3}	1.79×10^{-5}	0.003	−0.008
45.138	44.992	2.02×10^{-2}	2.00×10^{-2}	7.86×10^{-5}	0.004	−0.007
50.107	49.984	2.75×10^{-1}	2.73×10^{-1}	9.07×10^{-4}	0.003	−0.006

Doppler effect. The result is quite good but not enough to reach even a 1 K precision, especially at a low temperature where the signal-to-noise ratio decreases. The second method is well known to spectroscopists looking at the shape of R or P branches, which results from the Maxwell distribution of the fundamental state. This method can be simplified in our case, by measuring the ratio of the integrated absorbances σ_1 and σ_2 of two transitions with different lower state energies. An example is given with the $R(0,A_1)$ and $Q^b(1,F_1)$ transitions at 4333.669 and 4324.9331 cm^{-1}, respectively. T can be derived from the following equation

$$\ln\left(\frac{\sigma_1}{\sigma_2}\right) = \ln\left(\frac{S_1(T)}{S_2(T)}\right)$$
$$= \ln\left(\frac{S_1(T_0)}{S_2(T_0)}\right) - (E_1 - E_2) \times \left(\frac{1}{kT} - \frac{1}{kT_0}\right) \quad (21)$$

where E_1 and E_2 are the energies of the lower level (fundamental state) of transitions 1 and 2 (accurately measured by rotational spectroscopy) and $S_1(T_0)$ and $S_2(T_0)$ the oscillator strength at $T_0 = 296$ K. Unfortunately, the uncertainties on σ_1 and σ_2 and those on $S_1(T_0)$ and $S_2(T_0)$ were not low enough to reach uncertainties in the range of 1 K for the temperature.

Accurate values of the transition strengths $S_{\eta\eta'}$ are required not only to derive temperature but also to obtain reliable pressure. Only nine transitions were used in the study; more lines could be used in the relevant temperature range if their transition strengths are confident. On the other hand, one can imagine reversing the problem and using the low-temperature saturated vapor pressure spectra recorded at high resolution to increase the accuracy of some transition strengths. In particular, transitions corresponding to low J values are often better measured at low temperature, taking advantage of larger absorption, better resolution (Doppler effect), and less dense spectra (less blended transitions). Indeed, the work is continuing in this direction as such an improvement would be useful in the perspective of new space missions.[42]

Also, as mentioned in the text, the temperature of 40 K is a limit where the population ratio of the three nuclear spin isomers of methane starts to differ from its value at room temperature. Data analysis at lower temperatures would allow consideration of the nuclear spin conversion dynamics.[9]

CONCLUSIONS

In this paper, we have applied absorption spectroscopy techniques to probe gas-phase methane at temperatures below 91 K to deduce its Clapeyron solid–gas equilibrium curve. To this end, we used two distinct experimental setups.

The first one is a standard commercial "low resolution" spectrometer, which allowed us to measure the Clapeyron curve in the range 53–77 K and demonstrate that it is possible to derive this type of data at low pressures (down to $\sim 10^{-1}$ Pa for methane) and temperatures using a spectrometer that is not generally used to characterize the gas phase. This limit corresponds to the limit of detection raised by standard manometric measurements according to Fray et al.[43] In that study, it is claimed that several molecules have none or poor measurements of the $p(T)$ law in that pressure domain (C_2H_2, $CH_2=C=CH_2$, C_6H_6, HCN, etc.) and that the empirical relations deduced at higher pressures cannot be extrapolated to lower temperatures. With a low resolution setup it becomes

possible to extend our knowledge of the saturation pressure curve for many molecules of astrophysical interest.

A second setup used a homemade high-resolution laser source at 2.3 μm performing high sensitivity absorption measurements, which yielded novel data in the thermal range 40–50 K (with p down to $\sim 10^{-3}$ Pa) increasing by 2 orders of magnitude the validity of the Clapeyron law. On the other side, it is possible to measure pressure up to 70 K, by choosing transitions with low line strength S as soon as this value is known with enough precision.

With the two techniques, we were able to provide reliable and precise information about the methane vapor pressure in the 40–91 K range corresponding to a pressure variation of 7 orders of magnitude. We have shown that this in situ method is more convenient than standard manometric measurements. Reasons include the absence of the transpiration effect, which typically occurs when using gauges and also that the measurement of the targeted molecular density is not sensitive to any impurity.

APPENDIX

Determination of the Path Length in the LRS

The precise optical path length, L_{LRS}, was needed to model the spectra recorded with the low-resolution setup. For the high-resolution setup, this length has been determined in a previous work: $L_{HRS} = 692 \pm 5$ cm.[17] For the LRS, we introduced methane progressively into the cell from 0.755 up to 6.938 Torr at a temperature of 76.19 K, recording spectra corresponding to each pressure. The spectra of the $\nu_2 + \nu_3$ band are displayed in Figure 14a, where only the R(0) and R(1) lines correspond to an isolated transition. Figure 14c displays for each of the six pressures the difference between experimental and modeled spectra, defined above, and varying the path length L_{LRS}. Each curve has a minimum situated between 1.711 and 1.781 cm. From that, we have determined that $L_{LRS} = 1.746 \pm 0.035$ cm. Figure 14b displays the simulated spectra corresponding to the minima of Figure 14c. We see that the agreement is satisfactory.

AUTHOR INFORMATION

Corresponding Author
*E-mail: cermak@fmph.uniba.sk.

ORCID
Peter Čermák: 0000-0002-9746-1983
Stéphane Coussan: 0000-0002-0275-7272
Jennifer A. Noble: 0000-0003-4985-8254

Notes
The authors declare no competing financial interest.
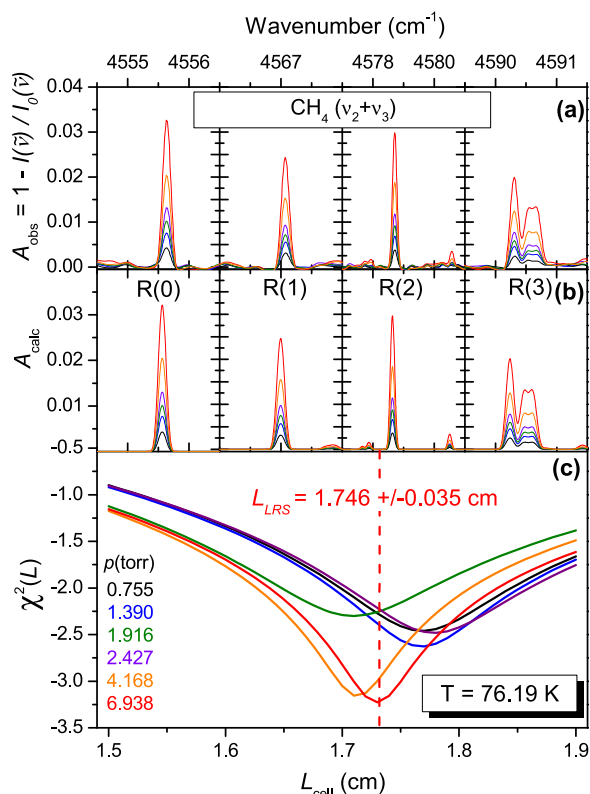
ACKNOWLEDGMENTS

Figure 14. Determination of the optical path length of the absorption cell used with the LRS. Plot (a) shows experimental absorption, whereas plot (b) shows the best simulated absorption obtained for six pressures between 0.755 and 6.938 Torr at 76.19 K. Plot (c) shows the χ^2 difference between experimental and modeled spectra.

■ REFERENCES

(1) Chandra, V. *Fundamentals of Natural Gas: An International Perspective*; PennWell Corp., 2006.

(2) Chynoweth, D. P.; Owens, J. M.; Legrand, R. Renewable Methane from Anaerobic Digestion of Biomass. *Renewable Energy* **2001**, *22*, 1−8.

(3) Wuebbles, D. J.; Hayhoe, K. Atmospheric Methane and Global Change. *Earth-Sci. Rev.* **2002**, *57*, 177−210.

(4) Lutz, B. L.; Owen, T.; Cess, R. D. Laboratory Band Strengths of Methane and their Application to the Atmospheres of Jupiter, Saturn, Uranus, Neptune, and Titan. *Astrophys. J.* **1976**, *203*, 541−551.

(5) Cordier, D.; Mousis, O.; Lunine, J. I.; Lavvas, P.; Vuitton, V. An Estimate of the Chemical Composition of Titan's Lakes. *Astrophys. J.* **2009**, *707*, L128−L131.

(6) Formisano, V.; et al. Detection of Methane in the Atmosphere of Mars. *Science* **2004**, *306*, 1758−1761.

(7) Daudé, B.; Elandaloussi, H.; Janssen, C. On the Gas Dependence of Thermal Transpiration and a Critical Appraisal of Correction Methods for Capacitive Diaphragm Gauges. *Vacuum* **2014**, *104*, 77−87.

(8) Bielska, K.; Havey, D. K.; Scace, G. E.; Lisak, D.; Harvey, A. H.; Hodges, J. T. High-Accuracy Measurements of the Vapor Pressure of Ice Referenced to the Triple Point. *Geophys. Res. Lett.* **2013**, *40*, 6303−6307.

(9) Cacciani, P.; Cosléou, J.; Khelkhal, M.; Čermák, P.; Puzzarini, C. Nuclear Spin Conversion in CH_4: A Multichannel Relaxation Mechanism. *J. Phys. Chem. A* **2016**, *120*, 173−182.

(10) Setzmann, U.; Wagner, W. A New Equation of State and Tables of Thermodynamic Properties for Methane Covering the Range from the Melting Line to 625K at Pressures up to 100 MPa. *J. Phys. Chem. Ref. Data* **1991**, *20*, 1061−1155.

(11) Eucken, A.; Karwat, E.; Fried, F. Die Konstantei der Thermodynamischen Dampfdruckgleichung bei Mehratomigen Molekeln. *Z. Phys.* **1924**, *29*, 1−35.

(12) Armstrong, G. T.; Brickwedde, F.; Scott, R. Vapor Pressures of Methanes. *J. Res. Natl. Bur. Stand.* **1955**, *55*, 39−52.

(13) Tickner, A. W.; Lossing, F. P. The Measurement of Low Vapor Pressures by Means of a Mass Spectrometer. *J. Phys. Chem.* **1951**, *55*, 733−740.

(14) "Methane—Phase Change Data" in NIST Chemistry WebBook, NIST Standard Reference Database Number 69. http://webbook.nist.gov (accessed June, 2018).

(15) Colwell, J. H.; Gill, E. K.; Morrison, J. A. Thermodynamic Properties of CH_4 and CD_4. Interpretation of the Properties of the Solids. *J. Chem. Phys.* **1963**, *39*, 635−653.

(16) Mondelain, D.; Camy-Peyret, C.; Mantz, A. W.; Tang, E.; Valentin, A. Performance of a Herriott Cell, Designed for Variable Temperatures between 296 and 20 K. *J. Mol. Spectrosc.* **2007**, *241*, 18−25.

(17) Čermák, P.; Cacciani, P.; Cosléou, J.; Khelkhal, M.; Hovorka, J.; Jeseck, P.; Michaut, X.; Moudens, A.; Fillion, J.-H.; Bertin, M.; et al. Observation of Methane Nuclear Spin Isomers in Gas Phase at Low Temperature. *J. Mol. Spectrosc.* **2012**, *279*, 37−43.

(18) Gordon, I.; Rothman, L.; Hill, C.; Kochanov, R.; Tan, Y.; Bernath, P.; Birk, M.; Boudon, V.; Campargue, A.; Chance, K.; et al. The HITRAN2016 Molecular Spectroscopic Database. *J. Quant. Spectrosc. Radiat. Transfer* **2017**, *203*, 3−69.

(19) Rothman, L.; Rinsland, C.; Goldman, A.; Massie, S.; Edwards, D.; Flaud, J.-M.; Perrin, A.; Camy-Peyret, C.; Dana, V.; Mandin, J.-Y.; et al. The HITRAN Molecular Spectroscopic Database and HAWKS (HITRAN Atmospheric Workstation): 1996 Edition. *J. Quant. Spectrosc. Radiat. Transfer* **1998**, *60*, 665−710.

(20) HITRAN Online. http://www.hitran.org (accessed June, 2018).

(21) Manca, C.; Martin, C.; Allouche, A.; Roubin, P. Experimental and Theoretical Reinvestigation of CO Adsorption on Amorphous Ice. *J. Phys. Chem. B* **2001**, *105*, 12861−12869.

(22) Harris, F. On the Use of Windows for Harmonic Analysis with the Discrete Fourier Transform. *Proc. IEEE* **1978**, *66*, 51−83.

(23) Georges, R.; Michaut, X.; Moudens, A.; Goubet, M.; Pirali, O.; Soulard, P.; Asselin, P.; Huet, T.; Roy, P.; Fournier, M.; et al. Nuclear Spin Symmetry Conservation in $^1H_2^{16}O$ Investigated by Direct Absorption FTIR Spectroscopy of Water Vapor Cooled Down in Supersonic Expansion. *J. Phys. Chem. A* **2017**, *121*, 7455−7468.

(24) Stohner, J.; Quack, M. *Handbook of High-Resolution Spectroscopy*; John Wiley & Sons, Ltd., 2011; pp 263−324.

(25) Verhoeven, J. W. Glossary of Terms Used in Photochemistry (IUPAC Recommendations 1996). *Pure Appl. Chem.* **1996**, *68*, 2223−2286.

(26) Čermák, P.; Triki, M.; Garnache, A.; Cerutti, L.; Romanini, D. Optical-Feedback Cavity-Enhanced Absorption Spectroscopy Using a Short-Cavity Vertical-External-Cavity Surface-Emitting Laser. *IEEE Photon. Technol. Lett.* **2010**, *22*, 1607−1609.

(27) Cerutti, L.; Ducanchez, A.; Narcy, G.; Grech, P.; Boissier, G.; Garnache, A.; Tournié, E.; Genty, F. GaSb-based VCSELs Emitting in the Mid-Infrared Wavelength Range (2-3µm) Grown by MBE. *J. Cryst. Growth* **2009**, *311*, 1912−1916.

(28) Čermák, P.; Hovorka, J.; Veis, P.; Cacciani, P.; Cosléou, J.; Romh, J. E.; Khelkhal, M. Spectroscopy of $^{14}NH_3$ and $^{15}NH_3$ in the 2.3µm Spectral Range with a New VECSEL Laser Source. *J. Quant. Spectrosc. Radiat. Transfer* **2014**, *137*, 13−22.

(29) Grundy, W. The Temperature-Dependent Spectrum of Methane Ice I between 0.7 and 5 µm and Opportunities for Near-Infrared Remote Thermometry. *Icarus* **2002**, *155*, 486−496.

(30) Kobashi, K.; Okada, K.; Yamamoto, T. Theory of Phase Transitions in Solid Methanes. XI. Infrared and Raman Spectra of the ν_3 and ν_4 Modes in Phase II of Solid CH_4. *J. Chem. Phys.* **1977**, *66*, 5568−5577.

(31) Tennyson, J.; Bernath, P. F.; Campargue, A.; Császár, A. G.; Daumont, L.; Gamache, R. R.; Hodges, J. T.; Lisak, D.; Naumenko,

O. V.; Rothman, L. S.; et al. Recommended Isolated-Line Profile for Representing High-Resolution Spectroscopic Transitions (IUPAC Technical Report). *Pure Appl. Chem.* **2014**, *86*, 1931.

(32) Kochanov, V. On Systematic Errors in Spectral Line Parameters Retrieved with the Voigt Line Profile. *J. Quant. Spectrosc. Radiat. Transfer* **2012**, *113*, 1635−1641.

(33) Takaishi, T.; Sensui, Y. Thermal Transpiration Effect of Hydrogen, Rare Gases and Methane. *Trans. Faraday Soc.* **1963**, *59*, 2503.

(34) Jacquinet-Husson, N.; Armante, R.; Scott, N.; Chédin, A.; Crépeau, L.; Boutammine, C.; Bouhdaoui, A.; Crevoisier, C.; Capelle, V.; Boonne, C.; et al. The 2015 Edition of the GEISA Spectroscopic Database. *J. Mol. Spectrosc.* **2016**, *327*, 31−72.

(35) Rey, M.; Nikitin, A. V.; Bézard, B.; Rannou, P.; Coustenis, A.; Tyuterev, V. G. New Accurate Theoretical Line Lists of $^{12}CH_4$ and $^{13}CH_4$ in the 0-13400cm^{-1} Range: Application to the Modeling of Methane Absorption in Titan's Atmosphere. *Icarus* **2018**, *303*, 114−130.

(36) Yurchenko, S. N.; Tennyson, J. ExoMol Line Lists − IV. The Rotation−Vibration Spectrum of Methane up to 1500 K. *Mon. Not. R. Astron. Soc.* **2014**, *440*, 1649−1661.

(37) Ba, Y. A.; Wenger, C.; Surleau, R.; Boudon, V.; Rotger, M.; Daumont, L.; Bonhommeau, D. A.; Tyuterev, V. G.; Dubernet, M.-L. MeCaSDa and ECaSDa: Methane and Ethene Calculated Spectroscopic Databases for the Virtual Atomic and Molecular Data Centre. *J. Quant. Spectrosc. Radiat. Transfer* **2013**, *130*, 62−68.

(38) Birk, M.; Wagner, G.; Loos, J.; Mondelain, D.; Campargue, A. ESA SEOM-IAS Measurement Database 2.3 μm Region. https://doi.org/10.5281/zenodo.1009122 (accessed July, 2018).

(39) Somayajulu, G. R. New Equations for Enthalpy of Vaporization from the Triple Point to the Critical Point. *Int. J. Thermophys.* **1988**, *9*, 567−575.

(40) McDowell, R. S.; Kruse, F. H. Thermodynamic Functions of Methane. *J. Chem. Eng. Data* **1963**, *8*, 547−548.

(41) Wagner, W.; Riethmann, T.; Feistel, R.; Harvey, A. H. New Equations for the Sublimation Pressure and Melting Pressure of H_2O Ice Ih. *J. Phys. Chem. Ref. Data* **2011**, *40*, No. 043103.

(42) Harrison, J. J.; Bernath, P. F.; Kirchengast, G. Spectroscopic Requirements for ACCURATE, a Microwave and Infrared-Laser Occultation Satellite Mission. *J. Quant. Spectrosc. Radiat. Transfer* **2011**, *112*, 2347−2354.

(43) Fray, N.; Schmitt, B. Sublimation of Ices of Astrophysical Interest: A Bibliographic Review. *Planet. Space Sci.* **2009**, *57*, 2053−2080.